A coupled plasticity-damage cohesive-frictional interface for low-cycle fatigue analysis

F. Parrinello[a], I. Benedetti[a]

[a] *Department of Engineering, University of Palermo, Viale delle Scienze, 90128, Palermo, Italy*

Abstract

A novel thermodynamically consistent cohesive-frictional model for the analysis of interface degradation and failure under either monotonic quasi-static loading or cyclic loading in low-cycle fatigue problems is proposed.

Starting from the definition of a suitable Helmholtz energy density function, a phenomenological interface model is developed in the framework of plasticity and damage mechanics. In particular, a coupled plasticity-damage activation function is defined and employed together the consistent evolution rules to capture the evolution of damage and plasticity under the action of the external loads. Due to the specific features of such threshold and flow rules, the initiation and accumulation of damage under monotonic increasing loads is captured and accompanied by negligible plastic evolution, allowing to approximate pure damage-based cohesive laws. On the other hand, coupling associative plasticity and damage evolution allows linking the interface degradation in low-cycle fatigue processes to plastic hysteresis, on the basis of the phenomenological assumption that no infinite plastic flows may happen without microstructural transformation leading to loss of load bearing capability. The model also embodies a smooth transition from an initially cohesive to a residual frictional interface behaviour, governed by a Coulomb frictional activation function.

The developed formulation has been implemented and assessed for individual interfaces, highlighting consistent phenomenological behaviour. It has been then applied to the analysis of delamination and de-bonding in composite test cases, showing accuracy against experimental data and confirming its potential.

Keywords: Cohesive zone modelling; Low-cycle fatigue analysis; Damage; Elastic-plastic cohesive-frictional interface; Composite bonding

1. Introduction

Material degradation under cyclic loading is encountered in several engineering applications and it is often the main cause of functional or structural failure [1, 2]: typically, under such loading conditions, structural components may fail, after a certain number of cycles N, at levels of stress well below the static strength. In common engineering practice, the design of mechanical systems undergoing repeated loads is often carried out, still today, by employing semi-empirical relationships linking some loading parameters (e.g. mean load, load amplitude, etc.) to the maximum number of cycles N_f the considered component can withstand before failure, then identifying the concept of *fatigue life*. Examples of such semi-empirical approaches are those based on the employment of Goodman-type diagrams, Whöler S-N curves, or Basquin's power laws, see e.g. Ref.[1].

*Corresponding author

Email address: francesco.parrinello@unipa.it (F. Parrinello)

Although useful for design purposes, such empirical approaches require extensive testing and calibration and do not provide any description of the damage accumulated within the considered mechanical element. More recent approaches to fatigue analysis are based on the incorporation of concepts and tools from *continuum damage mechanics* (CDM) [3, 4, 5, 6] and/or *fracture mechanics* (FM) [7] into the analysis, which allow capturing the initiation and evolution of damage or predicting the propagation of existing cracks within the component under the action of cyclic loadings: *safe life* or *damage tolerant* design methodologies have been developed for example in the automotive and aerospace sectors starting from such phenomenological techniques. CDM and FM approaches to fatigue are typically based, respectively, on the employment of Peerlings degradation laws [8] or extensions of the Paris law [9].

The classical dichotomy between CDM- and FM-based approaches, which would entail a certain difference between crack initiation and crack propagation problems, has been reconciled within the framework of Cohesive Zone Modelling (CZM) [10] that, in his basic form, is now a well developed methodology for the analysis of damage initiation, de-cohesion and fracture processes over predefined surfaces. CZM is based on the representation of the mechanical interaction between two solids through traction-separation relationships that model the physical behaviour of the interface itself, which in general is the seat of complex physical phenomena related to the initiation, evolution and coalescence of damage; as mentioned, in its basic form, CZM is particularly suitable for the representation of processes evolving over pre-defined interfaces and it is then well suited and has been extensively employed for investigating the failure of bonded joints or the delamination of composite laminated components in the aerospace industry [11, 12, 13]. More recently however, more complex frameworks based on CZM have been developed to investigate crack initiation and propagation in continuum materials [14] or micro-structured materials [15, 16, 17, 18].

Several kinds of cohesive interface models have been developed in the literature and specific attention has been focused on the assessment of thermodynamic consistency. In Ref.[19] potential-based and non-potential-based models have been analysed, highlighting some non consistent physical behaviours for the latter ones, with negative dissipation or repulsive normal traction under mixed mode delamination. The behaviour of some traction separation laws under mixed-mode loading is analysed also in Refs.[20, 21]. In Ref. [22] a thermodynamically consistent model, based on the definition of a Helmholtz free energy functional, is defined as the evolution of the *van den Bosch et al* model [23]. In Ref.[24] a thermodynamically consistent cohesive-frictional formulation has been proposed, with a higher value fracture toughness associated with mode II than mode I, motivated with the presence of friction; cohesive laws with different mode I and mode II fracture energies have bee presented also in Refs.[25, 26, 27]. The thermodynamic consistency of the potential based model proposed in [28] has been investigated in [20]. The influence of friction on the mode II dissipation energy has been experimentally analysed under cycling loading in Ref.[29], it has been numerically simulated with a cohesive-frictional interface model in Refs.[30, 31], modified in refs.[26, 27] by suggesting the use of two independent values of fracture energies and extended in Ref.[32, 33] to large displacement analysis. An analytical solution for the mode II fracture energy in the 4ENF test with frictional effects has been developed in Ref.[34]. The frictional behaviour has been modelled in Ref.[35] through an elastic-plastic interface model in a multi-scale computational strategy for the analysis of masonry structures, and a coupled damage-plasticity model has been proposed in Ref.[36]. The interface damage law has been recently developed in an hybrid equilibrium based formulation in [37, 38] and in a multi-physics framework in [39, 40, 41].

The present study focuses on the development of a cohesive-frictional interface model for the analysis of low-cycle fatigue problems. Several works have been devoted to the analysis of interfaces undergoing cyclic loads: Nguyen *et al.* [47] considered the interface stiffness degradation in the reloading branch of the loading cycle, but it did not include it in a damage framework; Roe and Siegmund [48] adapted for cyclic loading analysis the law proposed by Needleman in Ref.[49]; Yang *et al.* [50] proposed to consider damage as a function of the accumulated plastic shear strain; Oller *et al.* [51] developed a CDM-based approach to fatigue analysis, linking the damage threshold to the number of cycles. Martinez *et al.* [52] addressed ultra-low-cycle fatigue problems using a plastic damage model where damage is linked to a strain softening parameter accounting for the volumetric fracture energy dissipated by the material; Carrara and De Lorenzis [53] proposed a coupled damage-plasticity formulation for the analysis of interfaces under cyclic shear loads, envisaging damage evolution only at the unloading plastic process; Carrata *et al.* [54] developed a phase-field approach for the analysis of fatigue in brittle materials, relating the material degradation to a cumulative history variable. Bocciarelli [55] proposes a pure damage model based on a free energy function governing the interface behaviour under monotonic load. The behaviour under cyclic loads is modelled with damage increments in the reloading branches and damage healing, or crack retardation, in the unloading ones. Neither damage activation conditions nor dissipation functions are considered.

The cohesive zone approach was employed in Ref.[56]for high-cycle fatigue analysis of structural adhesives. In this approach the cyclic accumulation of damage is modelled by a degradation function that does depend on the number of cycles, does not depend on the cycle amplitude, and it entails an interface strength reduction. Such formulation is not thermodynamically consistent; it was developed for and applied to pure mode I loading, it was modified in Ref.[57] for fatigue analysis under pure mode II loading and in Ref.[58] for mixed mode crack growth. In Ref.[59] the fracture process zone ahead of the crack tip was modelled by means of cohesive laws from which the energy release rate and the stress intensity factor were evaluated. The interface was kinematically modelled by the XFEM and the fatigue crack propagation was described by the Paris equation, which assumes the crack growth rate as a function of the stress intensity factor range in the cyclic load.

Most of the available approaches to low-cycle fatigue degradation are not developed within a thermodynamic framework and the definition of a Helmholtz free energy and the actual dissipation related to material degradation are neither defined nor estimated. Indeed, in most low-cycle formulations, cyclic degradation is often modelled resorting to Peerling-like laws [60], as a function of the cycle stress amplitude, mean stress and number of loading cycles, but no specific thermodynamically consistent evolution laws, functions of the state variables in the loading cycle, are employed.

In this work, novel thermodynamically consistent cohesive laws are proposed, starting from a suitably defined Helmholtz free energy function, where the material behaviour is governed by a point-wise set of state variables (plastic deformation, damage, internal variables, etc.). The traction components, the evolution of plastic and damage variables and the relevant constitutive equations are derived following the classical Coleman and Noll procedure [61]. The model satisfies the second law of thermodynamic so that dissipation is null for any elastic loading process and it is non-negative for any loading path involving plastic or damage increments.

The interface formulation proposes an original interpretation of the *micro-mechanical* behaviour of bonded materials, which undergo strength and stiffness degradation when the applied stress cycles below the material strength. Such an interpretation postulates a close relationship between plastic hysteretic dissipation and material irreversible degradation. This relationship is based on the observation that no solid material can dissipate energy without limits and that the plastic hysteretic dissipation produces also micro-mechanical bond breaking with the relevant strength and stiffness degradation. Such a complex behaviour has been phenomenologically modelled in the framework of coupled damage and plasticity, in a thermodynamic consistent formulation satisfying the first and second laws of thermodynamics: the approach differs from formulations that assume semi-empirical traction-separation relationships without any reference to thermodynamic consistency, which may result in unrealistic energy dissipation profiles. The relationship between cyclic degradation, energetic dissipation and fatigue life has been experimentally observed and reported in several works, see e.g. Refs.[62, 63].

In the literature, other authors have proposed energetically consistent formulations for fatigue problems. A consistent model for high-cycle fatigue life prediction of metallic materials was proposed e.g. in Ref[64]: it considers two different sets of internal variables, one set related with the reversible behaviour, such as plasticity, and the other one governing the irreversible evolution of damage; the cumulative damage is defined as a function of the dissipation and of the number of cycles N. Another consistent model for fatigue life prediction is proposed in Ref.[65], which is based on the Helmholtz free energy function. The damage evolution is defined in a rate form, as an exponential function of its conjugate variable, that is the energy release rate. Moreover, an energy-based model, but not developed in a thermodynamic framework, is proposed in Ref.[66], which accounts for the effects of mean stress and strain on the fatigue life of superelastic materials. However, the above-mentioned references are specifically addressed to *high-cycle* fatigue analysis and the evolution of damage is explicitly linked to the number of cycles N, which appears as an independent variable in the formulation. On the contrary, the novelty of the proposed formulation consists in the development of a framework for cycle-by-cycle analysis which is simultaneously thermodynamically consistent and employs a single set of material parameters for addressing the analysis of *both* monotonic *and* cyclic load cases.

The paper is organised as follows. The thermodynamically consistent formulation is described in Section 2, where the details about the damage activation and evolution rules, the plastic flow activation and evolution and the hysteretic coupling between plasticity and damage evolution are given. The formulation is then tested in Section 3, where the behaviour and degradation of an individual interface under monotonic and cyclic loads is assessed and discussed, before the application of the developed tool to the analysis of two case studies involving *a*) the de-bonding of a composite sheet glued to a concrete block and *b*) the analysis of delamination growth in a carbon/epoxy composite in a double cantilever beam test. A short summarising discussion about the proposed model, the obtained results and possible future extensions are reported in Section 4, before the *Conclusions*.

2. Coupled plasticity-damage frictional interface model

The present Section is devoted to the theoretical derivation of the proposed elastic-plastic cohesive-frictional law with irreversible damage evolution for interfaces undergoing cyclic mixed-mode loading.

2.1. Thermodynamic framework

The proposed model represents the interface progressive degradation employing a non-associative flow rule for damage evolution within the context of continuum plasticity theory and continuum damage mechanics. CDM is a widely employed framework for cohesive interfaces, as it provides suitable concepts and methods for the representation of de-cohesion and fracture processes [67, 68, 69, 42, 44]. Several cohesive interface models, see e.g. Refs.[70, 30, 36, 71, 45], are based on the classical definition of a scalar damage variable ω as

$$\omega := \frac{dS_c}{dS} = \frac{dS - dS_s}{dS} \tag{1}$$

where, in the neighbourhood of a generic point, dS is a measure of the reference *pristine* interface and dS_c represents the interface *failed* or *cracked* fraction.

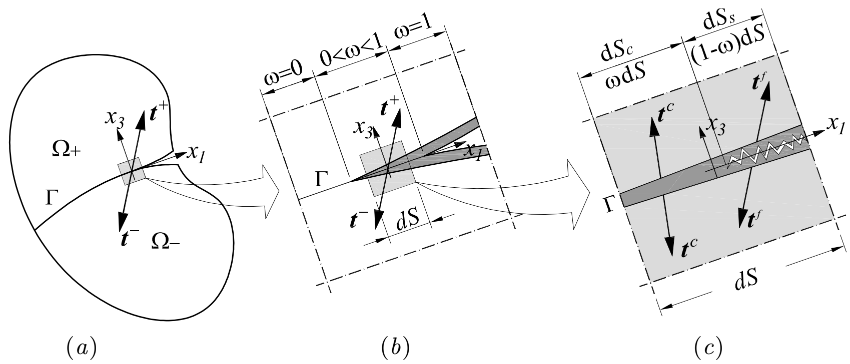

Figure 1: (a) Tractions $\boldsymbol{t}$ at the interface Γ connecting the solid domains Ω_+ and Ω_-; (b) *Process zone* with damage $0 < \omega < 1$ between the pristine zone with $\omega = 0$ and the cracked zone with $\omega = 1$; (c) *Mesoscale* model of a Representative Interface Element with its decomposition into the pristine and cracked fractions, dS_s and dS_c, highlighting the relevant cohesive and frictional tractions, $\boldsymbol{t}^c$ and $\boldsymbol{t}^f$.

The cohesive-frictional behaviour is modelled in the same *mesoscale* constitutive framework as that proposed by the Authors in Refs.[30, 26, 27] and represented in Fig.1, where cohesive interface behaviour, with traction $\boldsymbol{t}^c$, is assumed over the residual sound region $dS_s = dS - dS_c$ while frictional contact behaviour, with traction $\boldsymbol{t}^f$, is assumed over the cracked reagion dS_c. The proposed formulation also models the progressive transition from the initial cohesive behaviour of the pristine interface up to the residual frictional one of the fully damaged interface, to avoid pathological mechanical discontinuities, as discussed for example in Ref.[43].

In cohesive zone formulations, complete delamination and fracture are modelled by fully damaged interfaces, where $\omega = 1$ and two new surfaces exhibiting frictional contact behaviour are created; the full damage condition may also be employed to represent pre-existing cracks. On the other hand, the crack *initiation* phase is modelled by the evolution of the so called *process zone*, where the damage variable evolves within the interval of values $0 < \omega < 1$, as represented in Fig.(1). In the pristine condition, $\omega = 0$ over the whole interface Γ; under either monotonic or cyclic loading, damage within the process zone evolves and the process zone itself extends; cracks form when and where the full damage or failure condition $\omega = 1$ is attained within the process zone and the cracks propagate as the failed regions extend.

In cohesive zone modelling the de-cohesion process evolves along pre-determined zero-thickness interfaces, so that the kinematic variable adopted to quantify, in the surrounding of a generic interface point P, the separation of the solids meeting at the interface itself is the *displacement jump* vector, defined as

$$\boldsymbol{u} := [\![\boldsymbol{u}]\!] = \boldsymbol{u}^+ - \boldsymbol{u}^-, \tag{2}$$

where $\boldsymbol{u}^+$ and $\boldsymbol{u}^-$ are the displacements of the two physical points P^+ and P^-, belonging to the conventionally defined upper $(+)$ and lower $(-)$ faces of the opening interface and coinciding with the same point P in the pristine condition.

In this work, both an *extrinsic* cohesive law, in which the initial rigid response of the interface is replaced, upon the attainment of a certain threshold, by an elastic-plastic response with damage evolution, *and* an equivalent *intrinsic* counterpart have been implemented and assessed. The formulation is based on the assumption of a moving *endurance* surface in the space $\{t_1, t_2, t_3\}$ of the traction components, such that no material degradation under cyclic loading takes place for traction states within such surface. With the aim of developing the formulation within a thermodynamically consistent framework, the following Helmholtz free energy density function per unit surface

$$\psi(u_i, \alpha_i, \omega) := \frac{1-\omega}{2\,\omega}\left[K_i \left\langle u_i - u_i^p \right\rangle_n^2 + C_i \alpha_i^2\right] + \frac{1}{2} K_i^f \left(u_i - u_i^p \delta_{i3} - u_i^f\right)^2 \qquad i = 1, 2, 3 \tag{3}$$

is introduced, see e.g. Refs.[72, 26, 27], which plays the role of a potential with respect to external and internal state variables. In Eq.(3), the Einstein's summation convention is assumed, u_i are displacement jump components, being $u_3 = u_n$ the normal component, u_i^p identify residual displacement components at the interface upon complete un-loading, which can be considered as plastic components in the interface deformation process, u_i^f are frictional relative displacements, K_i denote elastic stiffness components, K_i^f are frictional stiffness components, C_i are hardening coefficients and α_i are kinematic hardening variables governing the position of the endurance surface. The frictional kinematic components u_i^f represent both the relative sliding displacements between the two faces of the damaged interface subjected to frictional tractions and their separation displacement, with associated null frictional traction, under opening conditions. The kinematic internal variables u_i^p, u_i^f and α_i are all assumed to be null in the initial pristine status. Additionally the operators

$$\left\langle f_i \right\rangle_n := \begin{cases} f_i & i = 1, 2 \\ \left\langle f_i \right\rangle_+ & i = 3 \end{cases} \tag{4}$$

have been employed, with the aim of accounting for the difference between the behaviour of the interface under tensile or compressive normal traction, where the Macaulay brackets $\langle \cdot \rangle_+$ select the positive part of their argument, and δ_{i3} denotes the Kronecker operator selecting the normal component.

Thermodynamic consistency with the second principle is enforced by the Clausius-Duhem inequality

$$\dot{D} = t_i \dot{u}_i - \dot{\psi} \geq 0, \tag{5}$$

which states the non-negativeness of the mechanical energy dissipation density. Considering the specific expression of ψ in Eq.(3), upon expansion of the term $\dot{\psi}$, Eq.(5) yields

$$\dot{D} = \left(t_i - \frac{\partial \psi}{\partial u_i}\right) \dot{u}_i - \frac{\partial \psi}{\partial \omega} \dot{\omega} - \frac{\partial \psi}{\partial u_i^p} \dot{u}_i^p - \frac{\partial \psi}{\partial u_i^f} \dot{u}_i^f - \frac{\partial \psi}{\partial \alpha_i} \dot{\alpha}_i \geq 0. \tag{6}$$

For purely elastic processes, the absence of damage evolution $\dot{\omega} = 0$, of plastic evolution $\dot{u}_i^p = \dot{u}_i^f = \dot{\alpha}_i = 0$ and of dissipation $\dot{D} = 0$ implies

$$t_i := \frac{\partial \psi}{\partial u_i} = \frac{1-\omega}{\omega} K_i \left\langle u_i - u_i^p \right\rangle_n + K_i^f \left(u_i - u_i^p \delta_{i3} - u_i^f\right) \tag{7}$$

$$t_i^c := -\frac{\partial \psi}{\partial u_i^p} = \frac{1-\omega}{\omega} K_i \left\langle u_i - u_i^p \right\rangle_n \qquad \text{with } t_3^c \geq 0 \tag{8}$$

$$t_i^f := \frac{\partial \psi}{\partial u_i^f} = K_i^f \left(u_i - u_i^p \delta_{i3} - u_i^f\right) \qquad \text{with } t_3^f \leq 0 \tag{9}$$

which define the *cohesive* traction components t_i^c (with $t_3^c \geq 0$) as the conjugate variable of the elastic deformations $u_i^e = \langle u_i - u_i^p \rangle_n$ and the *frictional* traction components t_i^f (with $t_3^f \leq 0$) as the conjugate variable of the frictional elastic deformations $u_i^{fe} = u_i - \langle u_i^p \rangle_c - u_i^f$ for the residual frictional strength.

In the normal frictional component $t_3^f := \partial\psi/\partial u_3^f = K_3^f \left(u_3 - u_3^p - u_3^f \right)$ in Eq.(9), the positive plastic deformation governs the continuous transition form the cohesive tensile traction to the compressive traction of the contact–closing condition, for both the pristine and damaged interface. The normal frictional traction component is neglected in the normal cohesive component $\partial\psi/\partial u_3^p = \frac{1-\omega}{\omega} K_3 \langle u_3 - u_3^p \rangle_n + K_3^f \left(u_3 - u_3^p - u_3^f \right)$ in Eq.(8), thanks to the position of positive normal cohesive traction and negative frictional one. Moreover, the assumed plastic activation condition, which will be discussed in Section 2.3, states the increment of normal plastic deformation only for positive cohesive normal traction, so that the frictional traction cannot produce dissipation for any increment of the plastic deformation, that is $t_i^f \dot{u}_i^p = 0$.

Eqs.(7–9) state the internal equilibrium $\boldsymbol{t} = \boldsymbol{t}^c + \boldsymbol{t}^f$ between the representative interface element and its pristine and cracked fractions and are defined under the assumption of null frictional traction under tensile normal loading. The absence of frictional response under tensile loading is implied not only by Eq.(9), but it is also required by the frictional-contact activation condition defined in Section 2.5. Summarising, the proposed cohesive-frictional model defines a pure cohesive behaviour under tensile normal loading and a combined cohesive-frictional behaviour under compressive normal loading, that is

$$\begin{array}{ll} \boldsymbol{t} = \boldsymbol{t}^c & \text{for } t_3 \geq 0, \\ \boldsymbol{t} = \boldsymbol{t}^c + \boldsymbol{t}^f & \text{for } t_3 < 0. \end{array} \tag{10}$$

Moreover, the normal component is purely cohesive in tensile traction, i.e. $t_3 = t_3^c$ for $t_3 > 0$, and it is purely frictional in compressive loading, that is $t_3 = t_3^f$ for $t_3 < 0$. Consistently, the constitutive model prevents the development of compressive plastic deformation ($u_3^p < 0$), which would erroneously entail the interpenetration of the two solids at the interface.

For dissipative processes, thermodynamic consistency dictates

$$\dot{D} = Y\dot{\omega} + t_i^c \dot{u}_i^p + t_i^f \dot{u}_i^f - t_i^0 \dot{\alpha}_i \geq 0, \tag{11}$$

obtained from Eq.(6) upon defining the *energy release rate*

$$Y := -\frac{\partial\psi}{\partial\omega} = \frac{1}{2\omega^2} \left[K_i \langle u_i - u_i^p \rangle_n^2 + C_i \alpha_i^2 \right], \tag{12}$$

and the *traction hardening components* t_i^0

$$t_i^0 := \frac{\partial\psi}{\partial\alpha_i} = \frac{1-\omega}{\omega} C_i \alpha_i, \tag{13}$$

which provides the overall set of state equations. The presence of only positive normal components in Eq.(12), induced by the operator $\langle\cdot\rangle_n$, makes damage activation independent of the compressive component.

Eq.(11) identifies different contributions to the total dissipation $\dot{D}$: the contribution $Y\dot{\omega}$, energetically related to damage evolution; the term $t_i^c \dot{u}_i^p$, linked to the occurrence of plastic mechanisms;

the term $t_i^f \dot{u}_i^f$, coming from frictional strength; eventually, the term $t_i^0 \dot{\alpha}_i$ energetically emerging from interfacial microstructural re-organisation during kinematic plastic hardening.

The thermodynamic consistency of the proposed constitutive model with interface cyclic degradation is assured through specific activation conditions, with relevant flow rules under which the modelled non-linear processes produce positive dissipation. Pure damage evolution, plastic damage evolution and frictional sliding evolution are triggered by the following conditions:

- A pure damage activation condition, which initiates interface softening when the limit strength is attained;
- An elastic-plastic activation condition, couples with damage evolution, which governs plastic flow and interface stiffness and strength degradation;
- A Coulomb frictional contact condition, which represents the onset of frictional sliding of the partially or fully damaged interface.

Such activation conditions and the mechanics of the related processes are described in the next Sections.

2.2. Damage evolution modelling

The activation of pure damage at an interface is governed by the activation function

$$\phi_d = \frac{Y}{Y_0} - 1 \leq 0, \tag{14}$$

where Y_0 denotes a constant energy threshold defined by

$$Y_0 = \frac{1}{2} K_n^{-1} {t_n^d}^2, \tag{15}$$

where $K_n = K_3$ represents an interface normal stiffness-like term and t_n^d is the interface *cohesive tensile strength* in the case of pure damage, when no plastic processes are activated.

For pristine materials the definition of energy release rate given in Eq.(12) would be indeterminate, being $\omega = 0$. However, such formal indeterminacy can be overcome by inverting Eq.(8) and expressing Y as a function of the traction components, as

$$Y = \frac{1}{2(1-\omega)^2} \left[K_i^{-1} t_i^{c2} + C_i^{-1} {t_i^0}^2 \right], \tag{16}$$

and the damage activation function as

$$\phi_d = \frac{1}{(1-\omega)^2} \left[K_i^{-1} t_i^{c2} + C_i^{-1} {t_i^0}^2 \right] \frac{K_n}{{t_n^d}^2} - 1 \leq 0, \tag{17}$$

which allows identifying, in the traction space $\{t_1, t_2, t_3\}$, a domain of admissible stress states whose boundary identifies the damage limit surface $\phi_d = 0$: points *within* such surface correspond to *unloading* or *re-loading* interface conditions, with no associated damage evolution, while points *on* the boundary may be associated, when specific flow rules are fulfilled, to *loading* conditions, with subsequent interface damage-softening. It is worth observing that, the energy release rate in Eq.(16) can also be expressed in terms of the so called *effective stress/traction* $\tilde{t}_i = t_i^c / (1-\omega)$ and the damage activation function in Eq.(17) can be written as function of the effective stress, as classically done in CDMs [5].

The damage variable plays the role of an isotropic softening parameter: from the geometric point of view, while increasing from the initial pristine condition $\omega = 0$, it acts by progressively reducing the size of the damage limit surface $\phi_d = 0$ in the tractions space $\{t_1, t_2, t_3\}$, up to collapsing it into the origin of the reference frame when the interface failure condition $\omega = 1$ is attained, see Fig.(2).

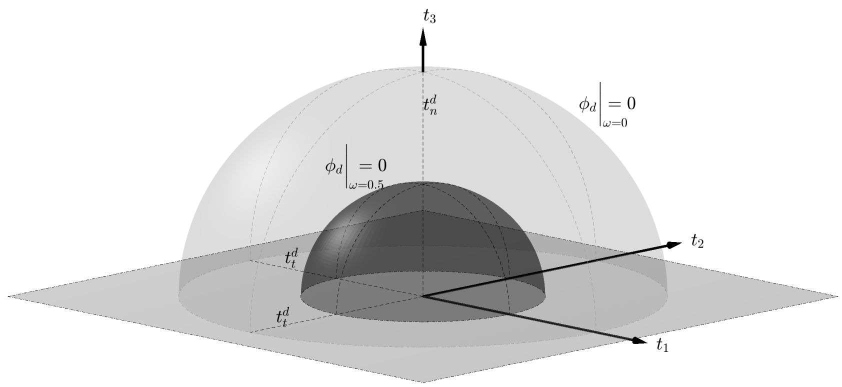

Figure 2: Graphical representation of the damage limit surface $\phi_d = 0$ in the semi-space of tensile traction $\{t_1, t_2, t_3\}$, both for the case of pristine interface status, $\omega = 0$, and for a damaged condition corresponding to $\omega = 0.5$.

Under increasing monotonic loads, the interface behaves elastically as long as $\phi_d < 0$, while pure damage evolution initiates when the threshold condition $\phi_d = 0$ is met, with the following associated flow rule

$$\dot{\omega} = \frac{\partial \phi_d}{\partial Y}\,\dot{\lambda}_d = \frac{\dot{\lambda}_d}{Y_0}, \tag{18}$$

and loading/un-loading/re-loading relationships

$$\dot{\lambda}_d \geq 0, \qquad \phi_d\,\dot{\lambda}_d = 0, \qquad \dot{\phi}_d\,\dot{\lambda}_d = 0, \tag{19}$$

where $\dot{\lambda}_d$ is the damage multiplier. The corresponding damage-induced dissipation can be evaluated considering that $\dot{\omega} > 0$ only if $\phi_d = 0$, thus implying

$$\dot{D}_d = Y\dot{\omega} = \dot{\lambda}_d \geq 0, \tag{20}$$

which confirms the unconditioned positiveness of the dissipation rate for any damage increment, being $\dot{D}_d = 0$ only if $\dot{\lambda}_d = 0$.

In the absence of plastic evolution, being $u_i^p = 0$ and $\alpha = 0$, the proposed cohesive model results in a bilinear response, analogous to that associated with pure damage models in the literature. Employing into Eq.(14) the expression of Y provided by Eq.(16), in the case of pure mode I debonding, being $t_n^c = t_n \geq 0$ and $t_t^c = t_t = 0$ and thus considering a pure cohesive behaviour, yields

$$\phi_d = \frac{1}{(1-\omega)^2}\left(\frac{t_n}{t_n^d}\right)^2 - 1 = 0 \quad \Rightarrow \quad t_n = (1-\omega)t_n^d, \tag{21}$$

which describes the loading softening branch of the cohesive law and confirms the value of $t_n = t_n^d$ as the traction threshold for damage activation for a pristine interface, $\omega = 0$. On the other hand, feeding into Eq.(14) the expression of Y given in Eq.(12), yields

$$\phi_d = \frac{1}{\omega^2}\left(\frac{K_n u_n}{t_n^d}\right)^2 - 1 = 0 \quad \Rightarrow \quad \omega = \frac{K_n u_n}{t_n^d}, \tag{22}$$

which provides the *critical opening displacement jump* $u_n^d = t_n^d/K_n$ at complete de-cohesion, when $\omega = 1$. In pure mode II, with $t_t^c = t_t > 0$, $t_t^f = 0$ and $t_n = 0$, evaluating the activation condition in Eq.(14) through Eq.(16) for Y and enforcing $\omega = 0$, allows identifying the *tangential strength* $t_t^d = t_n^d\sqrt{K_t/K_n}$, i.e. the threshold traction value for pure tangential loading. Viceversa, assuming $\omega = 1$ in the activation condition, Eq.(14), evaluated employing Eq.(12), allows identifying the *critical sliding displacement jump* as $u_t^d = t_n^d/\sqrt{K_n K_t} = u_n^d\sqrt{K_n/K_t} = t_t^d/K_t$ for pure mode II failure.

The expressions of the critical displacement jumps, for both pure mode I and II, define the parameters K_n and K_t appearing in the extrinsic formulation: although in extrinsic formulations, for which the response of the pristine interface is rigid, such terms may not be associated with a physical initial interface stiffness, their presence cannot be neglected in a thermodynamically consistent framework, as they provide a consistent definition of the energy release rate, i.e. the damage conjugate variable, and the relevant damage activation and evolution rules. On the other hand, the proposed extrinsic formulation can be straightforwardly recast and implemented in an intrinsic form, as detailed in Appendix A.

From the above relationships, it can be deduced that the same fracture toughness is associated with pure mode I and mode II failures, being $G_{\mathrm{I}} = \frac{1}{2}t_n^d u_n^d = \frac{1}{2}t_t^d u_t^d = G_{\mathrm{II}}$. However, different values of G_{I} and G_{II} could be considered within the considered framework by re-formulating the proposed damage model in a non-associative form, as done e.g. in Ref.[27], where two/three independent damage variables are considered for two/three-dimensional problems.

It is worth noting that the activation function ϕ_d governs static damage evolution at the interface limit strength, whereas cyclic degradation is accounted for by plastic hysteresis, governed by a different activation function, as it will be described in Section 2.3.

2.3. Elastic-plastic-damage evolution modelling

The interface degradation under cyclic loading is modelled resorting to a cohesive law with plastic hysteresis and associated damage. The hysteretic accumulation of damage is proposed to represent cyclic interface degradation related to complex dissipative mechanisms, such as crystallographic slip, frictional interactions between asperities, micro-cracking initiation etc.

Plastic hysteresis and the induced stiffness and strength degradation are modelled in the framework of associative damage and plasticity by introducing, in the space $\{t_1, t_2, t_3\}$, the coupled plastic-damage activation condition

$$\phi_p\left(t_i^c, t_i^0, Y\right) := \sum_{i=1}^{3}\left(\frac{t_i^c - t_i^0}{r_i}\right)^2 - 1 + a\left(\frac{Y}{Y_0}\right)^m \leq 0, \tag{23}$$

where $0 < a < 1$ is a plasticity-damage coupling parameter and the parameter $m > 0$ governs the interface fatigue life.

The elastic-plastic limit condition $\phi_p = 0$ identifies the *endurance surface*, represented in the space $\{t_1, t_2, t_3\}$ in Fig.(3), for the case of a pure elastic-plastic model with no coupling between plasticity and damage, $a = 0$, by an ellipsoid with principal semi-axes r_1, r_2 and r_3 and centroid $\boldsymbol{t}^0$. In the figure, the endurance surface is represented both for the case of positive normal traction, when the interface traction components coincide with the cohesive tractions ($t_i = t_i^c$), and for negative normal traction, $t_3 < 0$, when the cohesive normal component is forced to be vanish, $t_3^c = 0$.

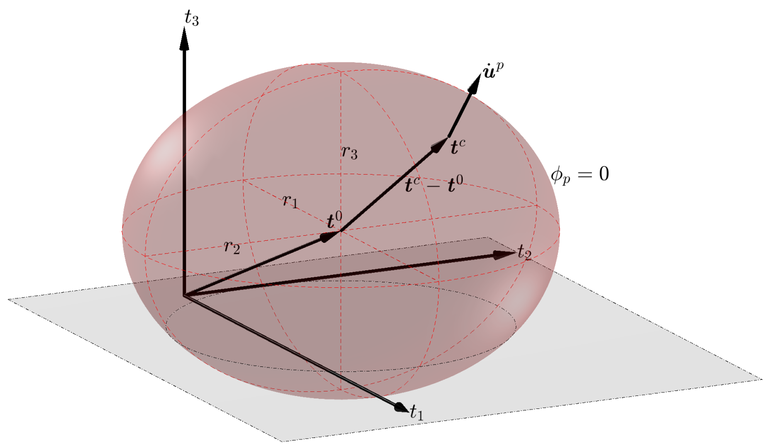

Figure 3: Graphical representation of the endurance surface in the space $\{t_1, t_2, t_3\}$ in the case of pure elastic-plastic behaviour ($a = 0$). The surface is an ellipsoid with principal semi-axes r_1, r_2 and r_3 and centroid $\boldsymbol{t}^0$. The latter one governs the kinematic hardening. Plastic and kinematic hardening evolution takes place ($\dot{\boldsymbol{u}}^p \neq 0$) only when the current traction vector $\boldsymbol{t}$ lies over the surface $\phi_p = 0$.

The evolution of the plastic and damage variables is governed by the following associative flow rules

$$\dot{u}_i^p = \frac{\partial \phi_p}{\partial t_i^c} \dot{\lambda}_p = 2\,\frac{t_i^c - t_i^0}{r_i^2}\,\dot{\lambda}_p, \tag{24}$$

$$\dot{\alpha}_i = -\frac{\partial \phi_p}{\partial t_i^0} \dot{\lambda}_p = 2\,\frac{t_i^c - t_i^0}{r_i^2}\,\dot{\lambda}_p, \tag{25}$$

$$\dot{\omega} = \frac{\partial \phi_p}{\partial Y} \dot{\lambda}_p = \frac{am}{Y_0} \left(\frac{Y}{Y_0}\right)^{m-1} \dot{\lambda}_p, \tag{26}$$

with the associated loading/un-loading/re-loading conditions

$$\dot{\lambda}_p \geq 0, \quad \phi_p \dot{\lambda}_p = 0, \quad \dot{\phi}_p \dot{\lambda}_p = 0, \tag{27}$$

where $i = 1, 2, 3$ and $\dot{\lambda}_p$ is the plastic multiplier.

Neither plastic hysteresis nor damage evolution is activated by stress states associated with points within the surface itself, for which $\phi_p \left(t_i^c, t_i^0, \omega\right) < 0$. The employment of tensile normal tractions in Eq.(23) prevents the development of plastic deformations under compressive loading. Cohesive laws are often assumed to be isotropic in the tangential plane $\{t_1 t_2\}$ so that $r_1 = r_2 = r_t$, $K_1 = K_2 = K_t$, $C_1 = C_2 = C_t$ and $r_3 = r_n$, $K_3 = K_n$, $C_3 = C_n$. In the case of fully isotropy, it follows that $r_i = r$, $K_i = K$, $C_i = C$, for $i = 1, 2, 3$.

The preposed formulation models only non-negative normal plastic deformation. In fact, under the assumptions of null initial plastic deformation and hardening variables, i.e. $u_i^p = 0$ and $\alpha_i = 0$

at $t = 0$, Eqs.(24-25) show that the kinematic hardening variables coincide with the plastic deformation, that is $u_i^p = \alpha_i$. Once the normal plastic deformation and normal hardening variables are or become zero, $u_3^p = \alpha_3 = 0$, Eq.(13) implies $t_3^0 = 0$, i.e. a null value of the normal static hardening variable. Thus, due to the assumption of non-negative cohesive traction normal component, $t^c \geq 0$, Eqs.(24-25) enforce non-negative increments of normal plastic deformation

$$\dot{u}_3^p = \dot{\alpha}_3 \geq 0 \quad \text{for } u_3^p = \alpha_3 = 0. \tag{28}$$

Moreover, neither plastic deformation nor damage degradation is influenced by compressive normal tractions.

By substituting Eqs.(15-16) into Eq.(26), the damage rate $\dot{\omega}$ can be expressed in terms of the traction components. For an interface subjected to cyclic tangential tractions only, with no normal stress ($t_n = 0$), the behaviour is purely cohesive ($t_t = t_t^c$) and the damage rate assumes the form

$$\dot{\omega} = \frac{am}{Y_0}\left[\left(\frac{1-\omega_0}{1-\omega}\right)^2 \frac{t_t^2 + {t_t^0}^2 K_t/C_t}{{t_t^d}^2}\right]^{m-1} \dot{\lambda}_p \tag{29}$$

where the hardening component t_t^0 can be considered as the mean stress of the loading cycle. The integration of the damage rate over the loading cycle yields an expression for the value of the damage increment per cycle analogous to the expressions used e.g. in Refs.[73, 74] to model fatigue life in a continuum damage model.

Considering that the flow rules imply $\dot{u}_i^p = \dot{\alpha}_i \neq 0$ and $\dot{\omega} > 0$ only if $\phi_p = 0$, it is possible to estimate the dissipation $\dot{D}_{pd} = \dot{D}_p + \dot{D}_d$ associated with the plasticity-damage activation employing Eqs.(24-26) into Eq.(11), which yields

$$\dot{D}_p = 2\sum_{i=1}^{3}\left(\frac{t_i^c - t_i^0}{r_i}\right)^2 \dot{\lambda}_p \geq 0, \qquad \dot{D}_d = am\left(\frac{Y}{Y_0}\right)^m \dot{\lambda}_p \geq 0, \tag{30}$$

which show the unconditioned positiveness of the dissipation rates for any plastic-damage increment, being both plastic and damage dissipations $\dot{D}_d = \dot{D}_d = 0$ only if $\dot{\lambda}_p = 0$, and positive otherwise.

2.4. Coupled elastic-plastic and damage limit conditions

The use of the elastic-plastic endurance surface allows associating a defined damage evolution with the cyclic process, both in the loading and in the un-loading branches of the loading cycles. Material softening is triggered by the fulfillment of *both* the damage *and* elastic-plastic activation conditions, $\phi_d = 0$ and $\phi_p = 0$. This state is represented in Fig.(4) in the case of tensile normal traction with pure cohesive behaviour, i.e. for $t_i^c = t_i$.

The plastic deformation and kinematic hardening still evolve according to Eqs.(24-25), while the damage progress is now governed by the sum of the two terms in Eqs.(18) and (26), that is

$$\dot{\omega} = \frac{\partial \phi_p}{\partial Y}\dot{\lambda}_p + \frac{\partial \phi_d}{\partial Y}\dot{\lambda}_d = \frac{am}{Y_0}\left(\frac{Y}{Y_0}\right)^{m-1}\dot{\lambda}_p + \frac{1}{Y_0}\dot{\lambda}_d \geq 0, \tag{31}$$

whereas the loading/un-loading/re-loading conditions are

$$\begin{aligned} &\dot{\lambda}_p \geq 0, \quad \phi_p \dot{\lambda}_p = 0, \quad \dot{\phi}_p \dot{\lambda}_p = 0, \\ &\dot{\lambda}_d \geq 0, \quad \phi_d \dot{\lambda}_d = 0, \quad \dot{\phi}_d \dot{\lambda}_d = 0. \end{aligned} \tag{32}$$

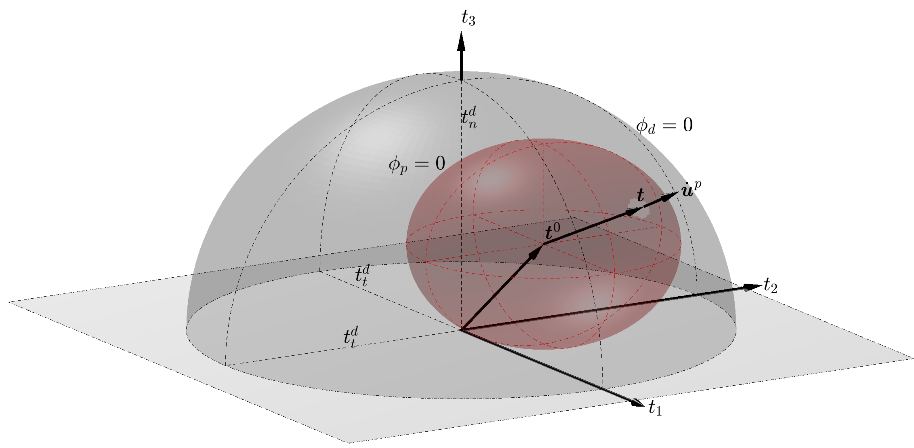

Figure 4: Graphical representation of both the endurance surface $\phi_p = 0$ and the damage limit surface $\phi_d = 0$ in the traction space $\{t_1, t_2, t_3\}$ for positive normal component. The fulfillment of the two activation conditions is represented by the tangent condition of the two surfaces at the current traction $\boldsymbol{t}$ and it governs the material softening.

The plastic dissipation $\dot{D}_p$ associated with the activation of the limit conditions is still defined by Eq.(30), while the damage dissipation is given by the sum of two different contribution as

$$\dot{D}_d = am \left(\frac{Y}{Y_0}\right)^m \dot{\lambda}_p + \dot{\lambda}_p \geq 0, \tag{33}$$

which again confirms the unconditioned positiveness of the dissipation rates and show that $\dot{D}_d = \dot{D}_p = 0$ only if $\dot{\lambda}_d = \dot{\lambda}_p = 0$. Moreover, while in the pure damage model the fracture toughness G_I coincides with the amount of damage dissipation in a complete de-cohesion process, in the coupled plasticity-damage model such condition is not verified and the damage dissipation is path dependent. Therefore, in a monotonic loading process, damage dissipation is nearly coincident with the assumed fracture toughness $G_I = G_{II}$, whereas in a cyclic loading process the total damage dissipation at failure (complete debonding) is generally lower than fracture toughness.

A direct relationship between energy dissipation and fatigue life has been assumed in Refs.[62, 63] with the dissipation measured in terms of temperature variation on the surface specimen during the cyclic load. Recently the fatigue life was experimentally predicted in Ref.[75] by the measurement of the energy consumption of an external heat source, which simulate the temperature profile of a specimen experiencing cyclic fatigue test. In the proposed formulation, the fatigue life is not strictly related to the mechanical dissipation, but the dissipation is positive for any plastic or damage increment and it can be correctly evaluated for any loading path.

Some considerations about the behaviour of the coupled plasticity-damage model under monotonic increasing loads are reported in Appendix B and numerically assessed in Section 3.1.1, where it is discussed how, due to limited accumulated plasticity under monotonic loads, the proposed formulation may approximate pure damage approaches, also providing a measure of interface strength.

2.5. Activation of the frictional-contact condition

The contact condition is statically defined in Eq.(9) which implies a non-positive value of the frictional normal traction, that is $t_3^f \leq 0$. The contact mechanics can be modelled resorting to the following opening activation condition

$$\phi_c\left(t_3^f\right) := t_3^f \leq 0, \tag{34}$$

which states that the interface opening displacement u_3^f increases when the opening activation condition is verified as equality, while it is defined in rate form by the following associative flow rule and opening/closing conditions

$$\begin{gathered}\dot{u}_3^f = \frac{\partial \phi_c}{\partial t_3^f}\dot{\lambda}_c = \dot{\lambda}_c \\ \dot{\lambda}_c \geq 0, \quad \phi_c\dot{\lambda}_c = 0, \quad \dot{\phi}_c\dot{\lambda}_c = 0,\end{gathered} \tag{35}$$

where $\dot{\lambda}_c$ is the opening displacement multiplier. The opening displacement is not a plastic deformation and does not induces any dissipation, being $t_3^f \dot{u}_3^f = \phi_c\dot{\lambda}_c = 0$.

The frictional behaviour of the fully or partially damaged interface under closing loading is modelled by a Coulomb frictional model in the framework of non-associative plasticity. The evolution of the frictional sliding displacements u_i^f of the interface edges is modelled by the frictional activation condition and frictional potential

$$\phi_f\left(t_i^f\right) := \left({t_1^f}^2 + {t_2^f}^2\right)^{1/2} + f \cdot t_3^f \leq 0 \tag{36}$$

$$\Omega_f\left(t_i^f\right) := \left({t_1^f}^2 + {t_2^f}^2\right)^{1/2}, \tag{37}$$

where f is the frictional coefficient. The evolution of the frictional sliding displacement is governed by the following flow rules and loading/un-loading/re-loading conditions

$$\begin{gathered}\dot{u}_i^f = \frac{\partial \Omega_f}{\partial t_i^f}\dot{\lambda}_f = \frac{t_i^f}{\left({t_1^f}^2 + {t_2^f}^2\right)^{1/2}}\dot{\lambda}_f \quad \text{for} i = 1, 2, \\ \dot{u}_3^f = \frac{\partial \Omega_f}{\partial t_3^f}\dot{\lambda}_f = 0 \\ \dot{\lambda}_f \geq 0, \quad \phi_f\dot{\lambda}_f = 0, \quad \dot{\phi}_f\dot{\lambda}_f = 0\end{gathered} \tag{38}$$

where $\dot{\lambda}_f$ the frictional multiplier. The rules in Eqs.(2.5) model also the sliding displacement under the opening condition, $t_3^f = 0$, which gives also, due to the frictional activation condition in Eq.(36), null tangential components, i.e. $t_1^f = t_2^f = 0$, and null frictional dissipation.

The limit condition $\phi_f = 0$ defines the classic conical frictional limit surface in the space of tractions $\{t_1, t_2, t_3\}$ with vertex at the reference frame origin. Fig.(5) shows a graphical representation of the conical frictional limit surface $\phi_f = 0$, the endurance surface $\phi_p = 0$ and illustrates the combined cohesive-frictional behaviour under compressive normal stress, with evolution of the tangential plastic deformation, with $\dot{u}_3^p = 0$, associated withthe cohesive behaviour and of the frictional sliding deformation, with $\dot{u}_3^f = 0$, associated with the frictional behaviour.

The dissipation associated with the frictional-contact behaviour can be computed from Eq.(11), which, considering the flow rules, yields

$$\dot{D}_f = \sum_{i=1}^{3} t_i^f \dot{u}_i^f = \left[\left(t_1^f\right)^2 + \left(t_2^f\right)^2 \right]^{1/2} \dot{\lambda}_f \geq 0, \tag{39}$$

which shows the unconditioned positiveness of the dissipation rate for any increment of frictional plastic deformation, and no dissipation, $\dot{D}_f = 0$, only if $\dot{\lambda}_f = 0$ or under opening loading.

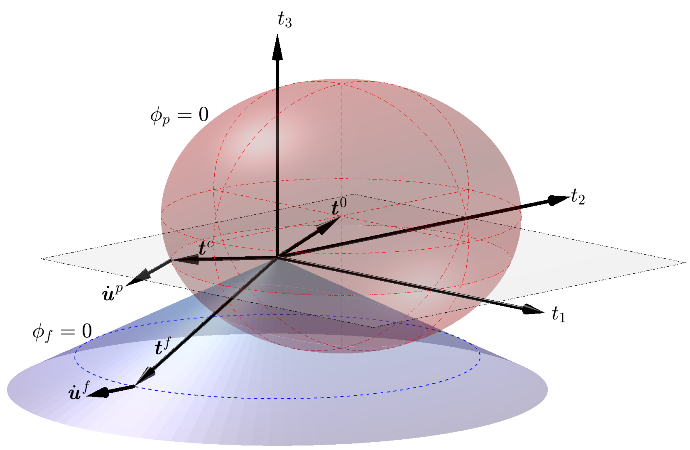

Figure 5: Graphical representation of both the endurance surface $\phi_p = 0$ and the frictional-contact surface $\phi_f = 0$ in the traction space $\{t_1, t_2, t_3\}$. Plastic evolution takes place ($\dot{\boldsymbol{u}}^p \neq 0$) only when the cohesive traction vector $\boldsymbol{t}^c$ lies over the endurance surface $\phi_p = 0$ and the frictional sliding takes place ($\dot{\boldsymbol{u}}^f \neq 0$) only when the frictional traction vector $\boldsymbol{t}^f$ lies over the frictional surface $\phi_f = 0$

3. Computational tests

In this section, the developed formulation is assessed and validated with reference to: a) an individual interface; b) an FRP-concrete pull test; c) a pure mode I delamination test on carbon/epoxy composite.

It is worth observing that the developed interface model is defined in the general framework of coupled plastic-damage mechanics and it is not devoted to the analysis of specific materials; depending on the set of constitutive parameters, the modelled behaviour can be mainly affected by damage or plasticity. Although the method could then be applied also to the analysis of metal interfaces, the presented numerical applications are limited to the analysis of debonding in composites. The proposed formulation has been implemented within the open source finite element software FEAP [76]. An intrinsic approach has been adopted, so that the interface elements exhibit initial elastic behaviour, with associated fictitious initial damage $0 < \omega_0 \ll 1$, according to the considerations expressed in Appendix A.

3.1. Individual interface tests

The behaviour of the individual interface is assessed first. The constitutive parameters of the assessed are collected Table 1, where the pure damage strength, the pure damage critical displacement jumps and the elastic stiffness parameters $K_n = K_t$ are defined by Eqs. (A.2) and (B.1) and by the conditions $u_n^d = t_n^d/K_n$ and $u_t^d = t_t^d/K_t$, and are function of the fracture toughness $G_{\mathrm{I}} = G_{\mathrm{II}}$, the elastic-plastic limit strengths $t_n^{pl} = t_t^{pl}$, the initial damage ω_0 and the plasticity-damage coupling parameter a. The hardening coefficients are assumed as $C_t = C_n = K_n/10$. Few numerical simulations, when explicitly stated, have been performed with other values of the coupling parameter, i.e. $a = 0.0001, 0.5$: in such cases, the sets of constitutive parameters are re-defined maintaining the same values of fracture toughness G_{I}, elastic-plastic limit strengths $t_n^{pl} = t_t^{pl}$ and initial damage ω_0.

Table 1: Interface properties for the single element numerical experiments.

Property	Components	Value
Interface properties		
Elastic-plastic limit strengths	t_n^{pl}, t_t^{pl}	10 MPa
Fracture toughness	G_{I}, G_{II}	$1\,\mathrm{N\,mm^{-1}}$
Interface constitutive parameters		
Pure damage strengths	t_n^d, t_t^d	27.3519 MPa
Pure damage critical displacement jumps	u_n^d, u_t^d	7.3121×10^{-2} mm
Endurance surface radii	r_n, r_t	2.0 MPa
Cohesive elastic stiffnesses	K_n, K_t	$393.7517\,\mathrm{N\,mm^{-3}}$
Cohesive hardening coefficients	C_n, C_t	$39.375\,17\,\mathrm{N\,mm^{-3}}$
Initial damage	ω_0	0.05
Damage-plasticity coupling parameter	a	0.05
Damage evolution parameter	m	1
Frictional coefficient	f	0.3

3.1.1. Monotonic loading tests

First, the behaviour of an individual interface under pure mode I or pure mode II monotonic loading in displacement control is assessed, initially assuming absence of friction, $\boldsymbol{t}^f = \mathbf{0}$, and pure cohesive traction, i.e. $\boldsymbol{t} = \boldsymbol{t}^c$. Due to the assumption of isotropic interface, the opening and sliding responses are numerically coincident and only the results for the pure mode I test are hereafter reported and discussed. The application of the developed formulation to monotonic loading is described in Appendix B.

The traction separation curve $t_n(u_n)$ provided by the proposed model is compared with the bilinear response provided by a model including only pure damage in Fig.6a, which confirms the relationship between the pure cohesive strength t_n^d and the elastic-plastic normal strength t_n^{pl} given by Eq.(B.1).

The whole traction-separation curve for the coupled plasticity-damage model is plotted in Fig.6b, together with the relevant evolution of the normal hardening parameter t_n^0 - the tangential hardening parameter remains zero - and a conventional representation of the endurance surface, or *curve* more rigorously in this case, at the pristine and the maximum strength states. It is worth recalling that the endurance surface is defined in the tractions space, so its representation in Fig.6b is meaningful only for the normal traction component and it highlights that the interface is elastic when the traction is internal to it and elastic-plastic with kinematic hardening when the traction is on the boundary of the endurance surface. The obtained numerical response is also compared to the analytical traction-separation law defined in Eqs.(B.2-B.5), confirming an almost perfect matching for the whole response, excluding the residual strength with pure damage softening, see Appendix B.

The thermodynamic consistency of the proposed formulation is confirmed by the analysis of the energies involved in de-cohesion process considered in the numerical test. The Clausius-Duhem inequality in Eq.(5) can be rewritten as

$$t_i \dot{u}_i = \dot{\psi} + \dot{D} \tag{40}$$

and, by time integration, the energy balance requires that the *external work*, defined as the amount of work done in the time interval $(0, t)$ by the applied traction

$$W^{ext}(t) = \int_0^t t_i \dot{u}_i d\tau, \tag{41}$$

be equal to the amount of *internal energy*

$$W^{int} = \psi + D_p + D_d + D_f, \tag{42}$$

where ψ is the Helmholtz free energy in Eq.(3) and

$$D_p = \int_0^t t_i^c \dot{u}_i^p d\tau, \qquad D_d = \int_0^t Y \dot{\omega} d\tau, \qquad D_f = \int_0^t t_i^f \dot{u}_i^f d\tau \tag{43}$$

are, respectively, the amount of plastic, damage and frictional dissipation.

The evolution of the energy contributions per unit interface area, i.e. the *surface energy density*, in the mode I de-cohesion process is shown in Fig.7a for a pure damage model, with no plastic dissipation and monotonically increasing linear damage dissipation. Due to the pure cohesive behaviour the frictional dissipation is not taken into account. The curves confirm the expected balance between external work and internal energy and show that the whole separation work coincides with the fracture toughness. On the other hand, the evolution of energy contributions involved in the de-cohesion process for the coupled plasticity-damage model is reported in Fig.7b, which confirms the thermodynamic consistency with the accurate balance between external work and internal energy. Damage dissipation at full de-bonding is coincident with the fracture toughness also for the coupled plasticity-damage model. Eventually, the work of separation, spent to take the interface to failure, is greater than the fracture toughness, due to the plastic dissipation, which is path dependent and cannot be univocally defined.

The total damage dissipation in a monotonic loading test is nearly coincident with the fracture toughness and it is almost independent on the coupling parameter a, as shown in Fig.8, where the numerical solutions obtained with the three different values $a = 0.0001,\ 0.05,\ 0.5$ are compared in terms of traction-separation curve and damage and plastic dissipation. The plot clearly represents the negligible influence of the coupling parameter on the monotonic response for values $0 < a < 0.5$. Conversely, the coupling parameter a has a significant effect in a cyclic loading condition, as shown in the next section.

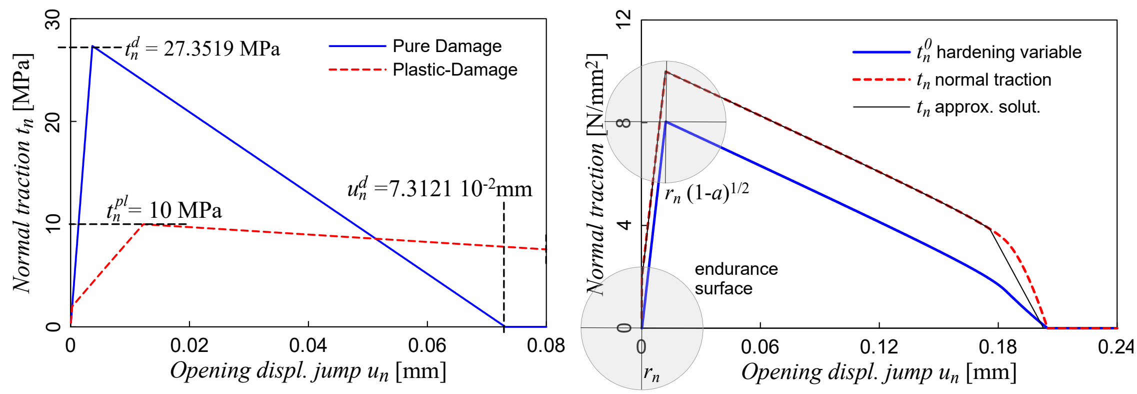

(a) (b)

Figure 6: Response $t_n = t_n(u_n)$ of the interface under mode I monotonic increasing loading in displacement control for: (a) The pure damage model and the coupled plasticity-damage model; the normal strength t_n^d, the critical displacement jump u_n^d of the bi-linear pure damage model and the elastic-plastic strength are highlighted. (b) The plasticity-damage model with the evolution of the normal hardening variable t_n^0 and a conventional representation of the endurance surface $\phi_p = 0$ at the pristine and maximum strength states. The analytical approximated traction-displacement solution is compared with the numerical one in Appendix B.

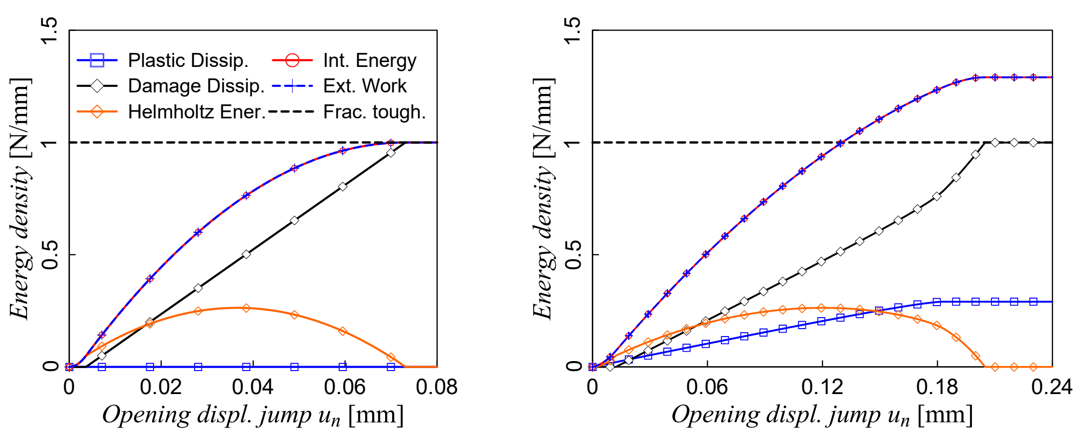

(a) (b)

Figure 7: Response of the interface under mode I monotonic increasing opening displacement for (a) the pure damage model and (b) the coupled plasticity-damage model in terms of plastic dissipation, damage dissipation, elastic strain energy, internal energy and external work. The value of the interface fracture toughness is also reported.

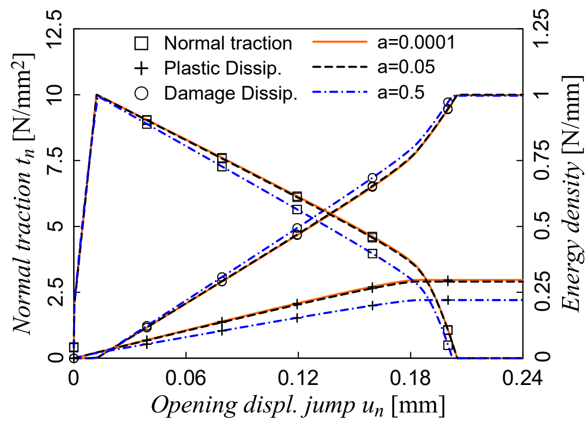

Figure 8: Response of the interface under monotonic increasing loading in displacement control, in pure mode I, for three values of the coupling parameter $a = 0.0001, 0.05, 0.5$. The interface responses are compared in terms of normal traction, damage dissipation and plastic dissipation. The symbol identifies the plotted data and the line type identifies the coupling parameter value.

3.1.2. De-cohesion test with un-loading/re-loading cycles

In this section, pure mode I and II loading tests including few unloading/reloading cycles are performed. The loading cycles, still performed in displacement control, imply the inversion of the traction signs and thus, in the case of mode I loading, compression.

The traction-separation curve $t_n(u_n)$ for the mode I test is shown in Fig.9a, where also the relevant evolution of the normal hardening parameter t_n^0 is represented: the hardening parameter identifies the centre of the endurance surface, or *curve*, which is represented for the state corresponding to the elastic portion of the first unloading branch. The elastic-plastic behaviour is associated with the kinematic hardening, which is related to the position of the endurance surface in the tractions space and affects its motion. The applied cyclic loading implies the inversion of the traction sign, with the subsequent activation of the pure elastic contact closing normal traction $t_n^f < 0$, without associated evolution of damage or plastic deformation.

The analogous traction-separation curve $t_t(u_t)$ for the mode II test is shown in Fig.9b, where, again, the evolution of the tangential hardening parameter t_t^0 is also reported. In this case, the interface exhibits pure cohesive behaviour, $\boldsymbol{t} = \boldsymbol{t}^c$, with no associated frictional traction, $\boldsymbol{t}^f = \boldsymbol{0}$, and the cyclic loading produces the inversion of the tangential traction sign, with larger hysteretic cycles and increment of damage and plastic deformation with respect to the mode I test.

The results of the cyclic tangential tests for three different values of the coupling parameter, namely $a = 0.001$, 0.05, 0.5, are compared in Fig.10 in terms of traction-separation curves, and in Fig.11a,b in terms of evolution of damage ω *vs* interface sliding displacement u_t, clearly showing that the higher the coupling parameter a the larger the damage increments during both the unloading elastic-plastic stage and the re-loading one. The detailed effect of the coupling parameter on the damage evolution for the first loading cycle is reported in Fig.11b.

The results of the cyclic tangential test, for the three values of the coupling parameter $a = 0.001$, 0.05, 0.5, are compared in Fig.12 in terms of interface density of damage dissipation D_d, plastic dissipation D_p and total dissipation $D_p + D_d$. Fig.12 shows that the amount of damage dissipation at full de-cohesion is lower than the fracture toughness and it decreases as the coupling parameter a increases, whereas it is nearly coincident with the fracture toughness in the monotonic loading test. Conversely, plastic D_p and total dissipation $D_p + D_d$ accumulate at each loading cycle and, at full de-cohesion, the total dissipation is greater than both the interface fracture toughness and the interface energy spent in the monotonic loading test, represented in Fig. 7b.

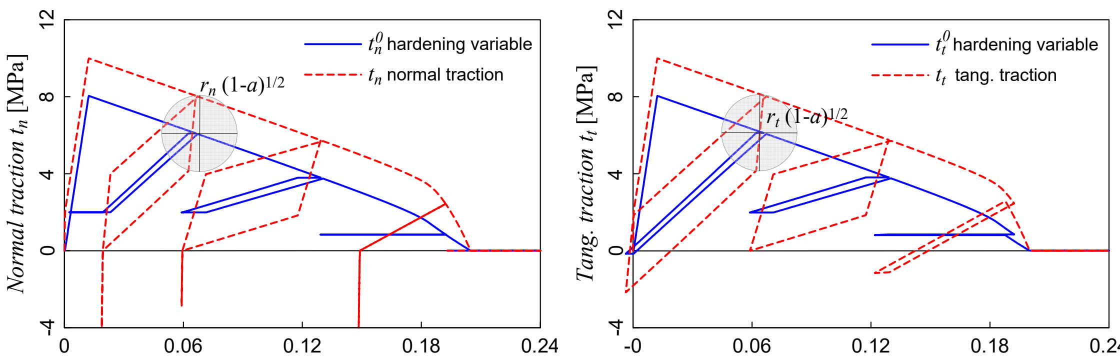

(a) (b)

Figure 9: Response of the interface under (a) pure mode I and (b) pure mode II loading with three un-loading/re-loading cycles. The elastic un-loading and re-loading branches are within the endurance surface, whose motion in the traction space is governed by the normal hardening variable t^0. Due to friction, the interface behaves elastically under pure compressive loads; on the contrary, its behaviour is elastic-plastic under negative or positive tangential loads.

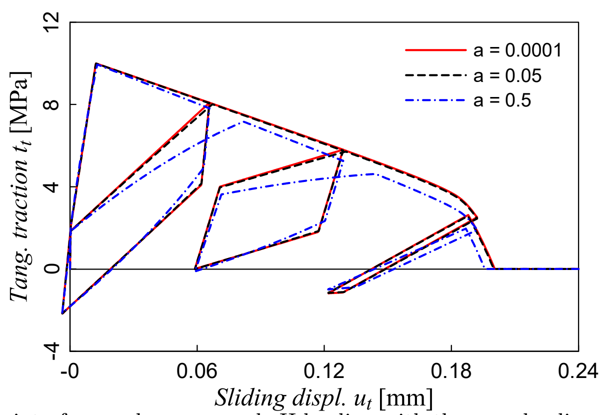

Figure 10: Response of the interface under pure mode II loading with three un-loading-re-loading cycles, in terms of traction-sliding curve $t_t\,(u_t)$, for three values of the coupling parameter $a = 0.0001$, 0.05, 0.5.

3.1.3. Frictional loading tests

The frictional contribution can be assessed by performing the monotonic and cyclic mode II tests presented in Sections 3.1.1 and 3.1.2 under constant compressive traction.

The traction-separation curve $t_t\,(u_t)$ for the frictional mode II monotonic test is reported in Fig.13a, with the decomposition of the interface total tangential traction into the cohesive and

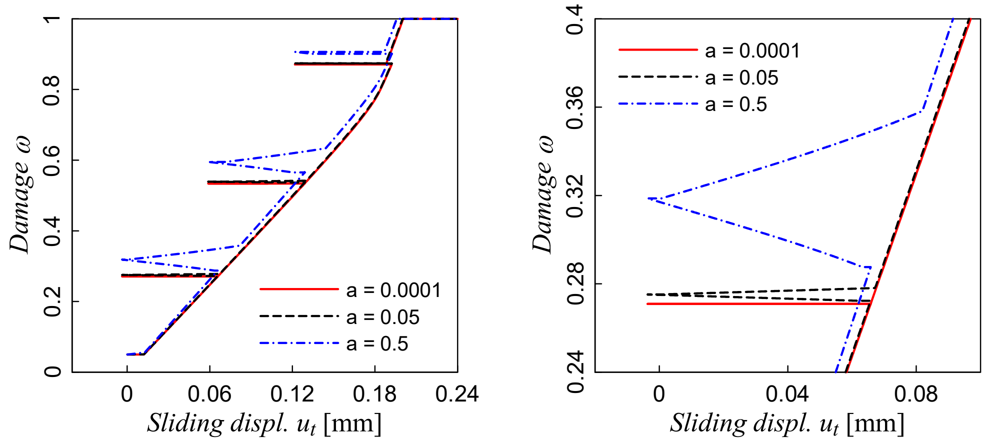

(a) (b)

Figure 11: Damage evolution under mode II loading with three un-loading-re-loading cycles, for the three values of the coupling parameter $a = 0.0001$, 0.05, 0.5: (a) damage evolution from pristine status up to failure. (b) detail of the of the first un-loading-re-loading cycle, represented within the inset in a.

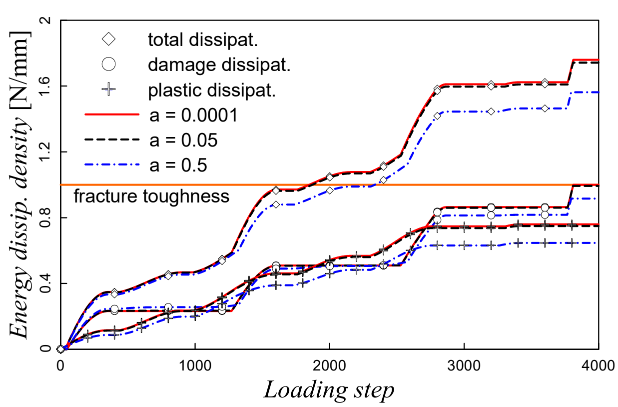

Figure 12: Energy dissipation surface density for the interface under mode II loading up to failure with three un-loading-re-loading cycles, and for the three values of the coupling parameter $a = 0.0001$, 0.05, 0.5. The graph shows the effect of the coupling parameter on damage, plastic and total dissipations: as the value of a increases, the dissipations decrease.

frictional contributions, i.e. $t_t = t_t^c + t_t^f$: the plot illustrates the evolution of the tangential traction and the smooth transition from the initial cohesive behaviour of the pristine interface to the pure residual frictional behaviour upon full de-cohesion.

The effectiveness of the proposed *cohesive-frictional* model is also confirmed by the numerical simulation of the interface interface element subjected to increasing tangential separation displacement with three un-loading/re-loading cycles, whose response is plotted and compared with the monotonic response in Fig.13b, which also reports the frictional tangential traction with the un-loading/re-loading cycles and the relevant frictional dissipation.

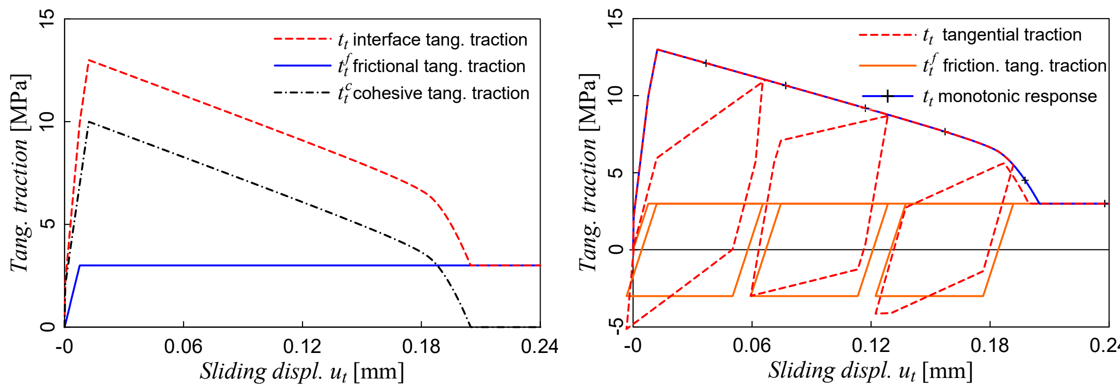

(a) (b)

Figure 13: Response of the interface under pure mode II loading condition in displacement control, with constant compressive loading $t_n = 10\,\mathrm{MPa}$, with: (a) Monotonic increasing load, in terms of total tangential traction t_t, cohesive tangential traction t_t^c and frictional tangential traction t_t^f. The graph highlights the frictional-cohesive behaviour of the interface under constant compressive normal stress and with the residual frictional strength. (b) Un-loading/re-loading cycles with increasing amplitude up to complete de-cohesion, in terms of tangential traction t_t and frictional tangential component t_t^f. The cyclic response is compared with the monotonic one.

3.1.4. Low-cycle fatigue analysis

The coupled plasticity-damage interface model is particularly suitable for the low-cycle fatigue analysis of bonded structures, for which the bonding surface often represents the preferential site of crack initiation and propagation.

In this section the low-cycle fatigue analyses are performed in load control for an individual interface element subjected to cyclic traction loading. The low-cycle numerical simulations are performed with the plasticity-damage coupling parameter set to $a = 0.1$; the other parameters are evaluated maintaining the elastic-plastic strengths set as $t_n^{pl} = t_t^{pl} = 10\,\mathrm{MPa}$ and the fracture toughness fixed as $G_{\mathrm{I}} = G_{\mathrm{II}} = 1\,\mathrm{N\,mm^{-1}}$. The damage evolution parameter is set to $m = 3$.

The results of the pure mode I analyses are reported in Fig.14a in terms of traction-separation curves, for four values of the traction cycle amplitude Δt_n and with the normal traction cycling between $t_n = 0$ and $t_n = \Delta t_n$. The four responses are shown only for the initial cycles and for the final ones, before interface failure, and are compared with the mode I monotonic response.

In load control, the interface suddenly fails when the traction reaches the residual strength of the damaged interface, which is defined as a function of the accumulated damage in Eq.(B.2) and it is graphically represented by the traction-separation curve of the monotonic response in Fig.14a. For the considered cyclic loading, the interface fails when $t_n = \Delta t_n$ and the value of the critical damage, i.e. the damage accumulated upon failure, can be estimated by rewriting Eq.(B.2) as a function of the normal traction, that is

$$\omega^{cr}(t_n) \approx 1 - \left[\frac{t_n^2 C_n + K_n \left(t_n - r_n \sqrt{1-a} \right)^2}{C_n {t_n^d}^2} \right]^{\frac{1}{2}} (1 - \omega_0) \,. \tag{44}$$

The values of the critical damage for the four cyclic tests are: $\omega^{cr} = 0.506$ for $\Delta t_n = 6\,\mathrm{MPa}$; $\omega^{cr} = 0.392$ for $\Delta t_n = 7\,\mathrm{MPa}$; $\omega^{cr} = 0.278$ for $\Delta t_n = 8\,\mathrm{MPa}$; $\omega^{cr} = 0.164$ for $\Delta t_n = 9\,\mathrm{MPa}$.

The interface damage evolution in the low-cycle tests, for the four values of traction cycle amplitude $\Delta t_n = 6, 7, 8, 9\,\mathrm{MPa}$, is shown in Fig.14b as a function of the number of loading cycles; in the same graph, also the interface fatigue life versus the stress amplitude Δt_n is reported, confirming the estimated values of the critical damage and the expected linear dependence, in the logarithmic scale, of the number of cycles to failure on the stress cycle amplitude. Such a dependence on the stress cycle amplitude is not affected by the possible occurrence of negative normal traction, for which the formulation assumes pure frictional behaviour. In particular, in a mode I low-cycle test, damage evolution is envisaged only when the interface is under tensile loading and not when it is in compression, as shown in Fig.15, where the numerical response of a cyclic *repeated* test, with $0 \leq t_n \leq \Delta t_n = 6\,\mathrm{MPa}$ is compared with the response of a *fully-reversed* test, with the normal traction cycling between $t_n = -6\,\mathrm{MPa}$ and $t_n = 6\,\mathrm{MPa}$. The numerical responses compared in Fig.15 exhibit the same non-linear behaviour and fatigue-life, although the stress amplitude in the fully-reversed test is twice that in the repeated test.

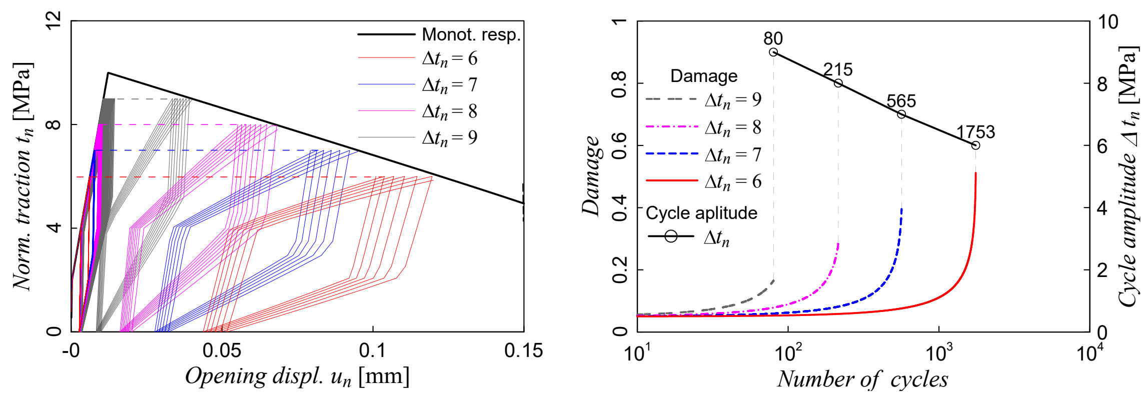

(a)

Figure 14: Response of the interface under repeated loading cycles in traction control, with normal traction cycling between $t_n = 0$ and $t_n = \Delta t_n$, with four different values of the load amplitudes Δt_n. (a) Traction-separation curves. (b) Damage evolution *vs* number of cycles and fatigue life in terms of number of cycles to failure *vs* cycle amplitude.

The modelled interface fatigue life is affected by the coupling plasticity-damage parameter a and by the damage evolution parameter m. To asses the influence of such parameters, a sensitivity analysis is performed by computing the interface fatigue life for pure mode I tensile tests, under traction cycles of amplitudes $\Delta t_n = 6, 7, 8, 9\,\mathrm{MPa}$, first setting $a = 0.1$ constant and considering

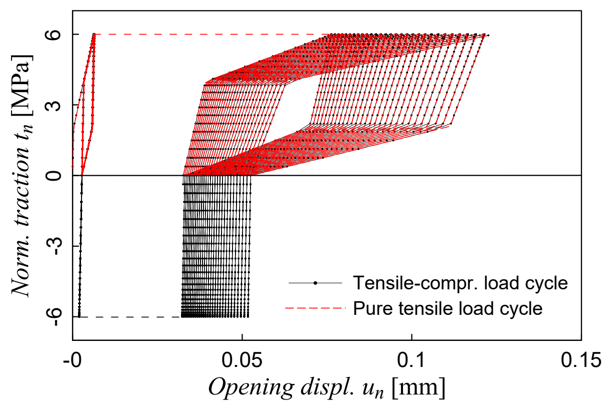

Figure 15: Pure mode I traction-separation curves of an interface element under loading cycles in traction control. A *repeated* tensile test, with $0 \leq t_n \leq \Delta t_n = 6\,\mathrm{MPa}$, is compared with a *fully-reversed* test, with the normal traction cycling between $-\Delta t_n$ and $+\Delta t_n$.

three different values $m = 1, 3, 5$ and then setting $m = 1$ constant and considering three values $a = 0.01, 0.05, 0.1$. In the parametric analysis, all the other constitutive parameters are defined keeping the values of the elastic-plastic strengths and of the fracture toughness constants, respectively set to $t_n^{pl} = t_t^{pl} = 10\,\mathrm{MPa}$ and $G_\mathrm{I} = G_\mathrm{II} = 1\,\mathrm{N\,mm^{-1}}$.

Figs.16a, b confirm the linear dependence, in the logarithmic scale, of the interface fatigue life on the stress cycle amplitude, and show how the parameter m affects the slope of the fatigue life curve whereas the parameter a translates the curve on the logarithmic plane with no or negligible effect on its slope. Eventually, the interface fatigue life is estimated under pure mode II loading, setting $a = 0.1$ and $m = 3$. Different values of the tangential traction cycle amplitude Δt_t are considered, namely $\Delta t_t = 3, 9, 10, 11, 12\,\mathrm{MPa}$, while the maximum tangential stress $t_{max} = \max(t_t)$ is kept constant as $t_{max} = 6\,\mathrm{MPa}$. The tests results for the performed low-cycle mode II tests are shown in Fig.17a, where the obtained traction-sliding curves are compared with the pure mode II monotonic response, and in Fig.17b, where the damage evolution *vs* the number of cycles and the interface fatigue life *vs* the stress amplitude Δt_t are reported.

Additionally, the interface fatigue life is evaluated for different values of the maximum tangential stress $t_{max} = 6, 7, 7.5, 8, 9\,\mathrm{MPa}$, keeping the loading cycles amplitude $\Delta t_t = 12\,\mathrm{MPa}$ constant. Fig.18a reports the tangential traction-sliding curves comparing them with the pure mode II monotonic response. Fig.18b shows the evolution of damage as a function of the number of loading cycles to failure and the interface fatigue life versus the maximum tangential stress t_{max}.

The results obtained about the interface fatigue life, reported in Figs.18b and 18b, show that the number of cycles to failure in the logarithmic scale is linearly dependent on the maximum traction t_{max} and it is much less dependent on the cycle amplitude Δt_t, excluding the cases for which $\Delta t_t \approx 2t_{max}$ and the pure elastic cycles with $\Delta t_t \leq r_t\sqrt{1-a}$. This result is probably related to the fact that both the critical damage, defined in Eq.(44), and the number of load cycles required to reach such critical damage are approximately inversely proportional to the maximum stress. The damage increment in the load cycle also depends on the cycle amplitude, but such dependence seems to be less relevant than that on the maximum stress. This feature has not emerged for the pure mode I fatigue tests, for which the *effective* cycle amplitude coincides with the maximum traction,

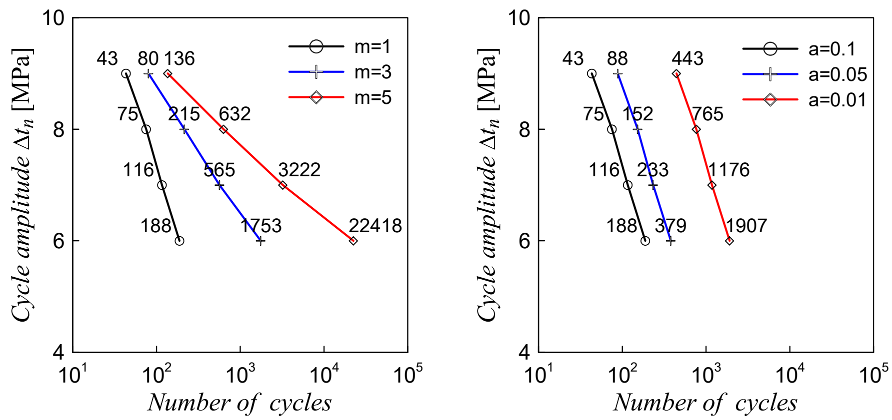

(a) (b)

Figure 16: Influence of the constitutive parameters a and m on the interface fatigue life, defined as the number of cycles to failure, for four values of the traction cycle amplitude: a) influence of the constitutive parameter m for $a = 0.1$; b) influence of the constitutive parameter a for $m = 1$.

while negative normal tractions do not affect the interface damage evolution.

The proposed formulation can model interface low-cycle fatigue degradation under any debonding condition, i.e. pure mode I, pure mode II or mixed mode. However, as discussed in Section 2.2, the model predicts the same fracture toughness $G_I = G_{II} = G$ independently of the mixed mode ratio. A thermodynamically consistent formulation with different and independent fracture energies associated to either mode I or mode II quasi-static monotonic loading has been developed by the authors in Refs.[26, 27]. However, such a formulation does not envisage any cyclic degradation; indeed, the formulation of a mixed-mode thermodynamically consistent model, *including* cyclic degradation, is an interesting but not trivial development of the present work and it is left for further investigations.

3.2. FRP-concrete pull test

In this section, the proposed formulation is validated for the analysis of de-bonding of a fibre-reinforced polymer (FRP) composite sheet glued to a concrete block. The reference experimental investigation was performed by Carloni *et al.* in Ref.[77], where a set of direct shear tests with classical pull configuration under either monotonic quasi-static or fatigue loading have been considered and analysed. Similar tests were considered in Refs.[53, 78]. The set-up and the dimensions of FRP-concrete pull test are represented in Fig.19, where the zoomed detail in the circle shows the sliding displacement between the FRP composite sheet and the concrete substrate, measured in the experimental tests. The thickness of the FRP composite sheet was $t = 0.167\,\mathrm{mm}$.

In the experimental investigation three monotonic tests were performed and it was found that the interface had an average interfacial fracture energy $G_{II} = 0.8\,\mathrm{N\,mm^{-1}}$ and an average shear strength $\tau^{max} = 6.43\,\mathrm{MPa}$. Three cyclic tests were also performed, with different values of the maximum and minimum applied load P. The first cyclic test, DS-F1 in Ref.[77], was performed with the load cycling between $P^{min} = 1.25\,\mathrm{kN}$ and $P^{max} = 6.0\,\mathrm{kN}$ and failure was reached after $n = 1290$ load cycles. The second cyclic test, DS-F2, was performed with the load cycling between

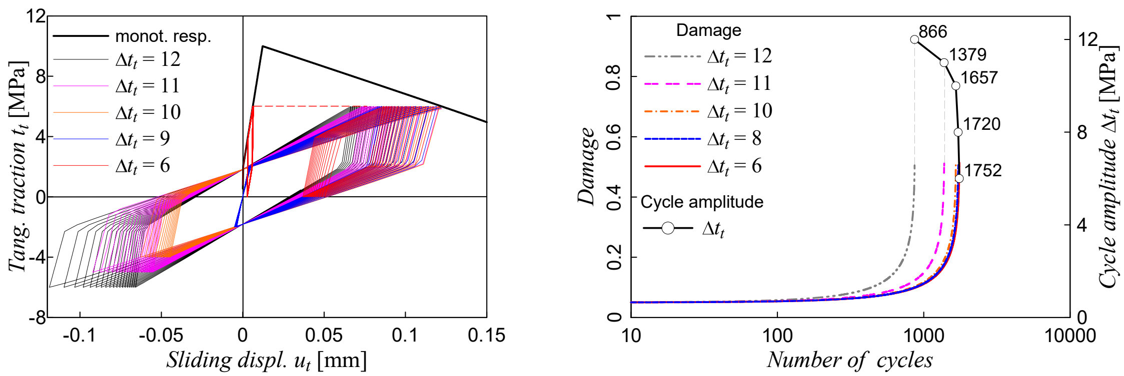

(a) (b)

Figure 17: Response of the interface element under pure mode II low-cycle fatigue analysis. The tests are performed with five values of the traction cycle amplitude $\Delta t_n = t_{max} - t_{min}$ and keeping the maximum tangential traction $t_{max} = 6\,\text{MPa}$ constant. (a) Traction-separation curves. Only the last loading cycles before interface failure are drawn, to avoid an excessively cramped representation. (b) Damage evolution *vs* number of cycles and fatigue life in terms of number of cycles to failure *vs* cycle amplitude.

$P^{min} = 1.1\,\text{kN}$ and $P^{max} = 5.1\,\text{kN}$ and failure was recorded after $n = 13192$ load cycles. In the third cyclic test, DS-F3, with $P^{min} = 1.1\,\text{kN}$ and $P^{max} = 4.5\,\text{kN}$, failure was recorded after $n = 116995$ cycles.

With the aim of validating it against the recalled experimental tests, the proposed interface constitutive model has been implemented into the open source finite element code FEAP [76], and the computational tests have been performed in a simplified two-dimensional test-case under plane stress condition. The concrete block and the composite sheet are discretized by nine-node linear elastic elements with Young modulus $E_c = 20\,\text{MPa}$ and Poisson ratio $\nu_c = 0.15$ for concrete and Young modulus $E_f = 230\,\text{MPa}$ and Poisson ratio $\nu_f = 0.15$ for the FRP composite sheet, respectively. The mesh elements of the concrete block and the composite sheet are connected by six-node interface elements and they are shown in Fig.20, where also the applied force and boundary conditions are schematically depicted. The experimental values of the fracture energy and shear strength have been used to calibrate the set of interface constitutive parameters collected in Table 2.

The numerical, analytical and experimental responses of the monotonic pull test are compared in Fig. 21 in terms of applied load P versus global slip, as represented in Fig. 19. The analytical solution of the monotonic FRP pull test has been proposed in Ref.[79] and developed in a simplified mono-dimensional formulation, under the hypothesis of rigid substrate and of interface with bi-linear constitutive response. The numerical test produces a maximum load lower than the experimental one; the same delamination load could be obtained assuming a value of the fracture energy greater than the one reported in Ref.[77], as done for example in Ref.[55]. However, observing that the fracture energy is generally considered as the most meaningful parameter in characterising interfaces delamination, all the simulations have been performed assuming the same value of fracture energy as that estimated in the reference experimental tests.

The numerical and experimental responses of the three cyclic pull tests DS-F1, DS-F2 and DS-F3

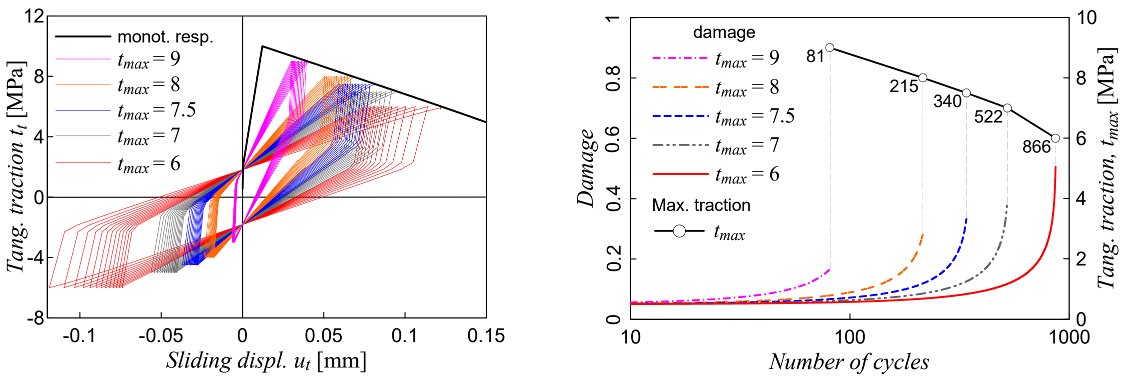

(a) (b)

Figure 18: Response of the interface element under pure mode II low-cycle fatigue analysis. The tests are performed with five values of the maximum tangential traction t_{max} and keeping the traction cycle amplitude $\Delta t_n = t_{max} - t_{min} = 12\,\text{MPa}$ constant. (a) Traction-separation curves. Only the last loading cycles before interface failure are drawn, to avoid an excessively cramped representation. (b) Damage evolution *vs* number of cycles and fatigue life in terms of number of cycles to failure *vs* cycle amplitude.

are compared respectively in Figs.22a-c , for some significant loading cycles. The first loading/unloading/re-loading cycle of the three numerical simulations are also drawn. The obtained results show good qualitative agreement between modelled behaviour and experimental data, with the same evolution of the stiffness degradation and the same amplitude of the hysteretic cycles, which is a measure of cyclic plastic dissipation. In fact, being the proposed model based on a thermodynamic formulation, the plastic dissipation coincides perfectly with the work done by the applied load P, as shown in Sections 3.1.1 and 3.1.2. Some differences between computations and experiments can be observed in terms of residual displacement at the minimum load and in terms of faster numerical stiffness degradation, with respect to the experimental one, at the beginning the cyclic pull test.

The proposed formulation can model and reproduce with remarkable accuracy not only the main phenomena involved in the interface delamination, such as the damage evolution with the associated stiffness degradation and the plastic dissipation related to the hysteretic behaviour, but it also provides an accurate estimate of the fatigue life of the composite-concrete interface, as shown in Fig.23, where in the number of cycles to failure versus load cycle amplitude ΔP is reported.

Eventually, the maps of tangential stress at the peak of load cycles 75, 575 and 1175 of the test DS-F1 are drawn in Fig.24.

3.3. Carbon/epoxy composite DCB test

In this section, the proposed formulation is validated for the analysis of pure mode I delamination of an end notched carbon/epoxy composite specimen in a classic Double Cantilever Beam (DCB) test. The reference experimental investigation was performed by Asp *et al* [80] on a specimen of width $b = 20\,\text{mm}$, single beam thickness $h = 1.55\,\text{mm}$ and artificial initial crack length $a_0 = 35\,\text{mm}$, as represented in Fig.25 . The composite elastic properties were: flexural elastic modulus $E_F = E_1 = 120\,000\,\text{MPa}$, transverse elastic modulus $E_T = E_2 = E_3 = 10\,500\,\text{MPa}$, shear moduli $G_{12} = G_{23} = 5250\,\text{MPa}$, $G_{23} = 3480\,\text{MPa}$ and Poisson ratios $\nu_{12} = \nu_{13} = 0.30$, $\nu_{23} = 0.51$. Finally,

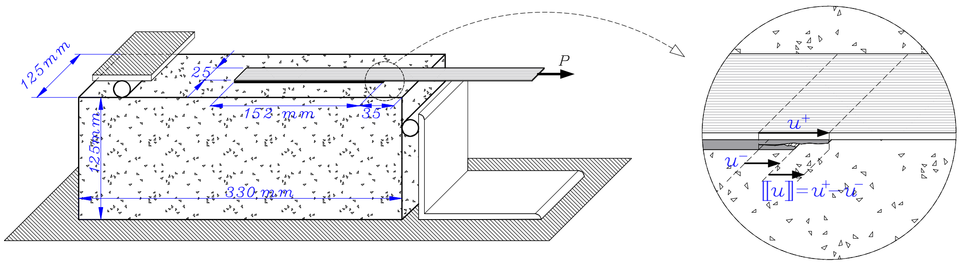

Figure 19: Set-up and dimensions of the of the FRP-concrete pull test. The zoomed detail in the circle shows the sliding displacement between the FRP composite sheet and the concrete substrate.

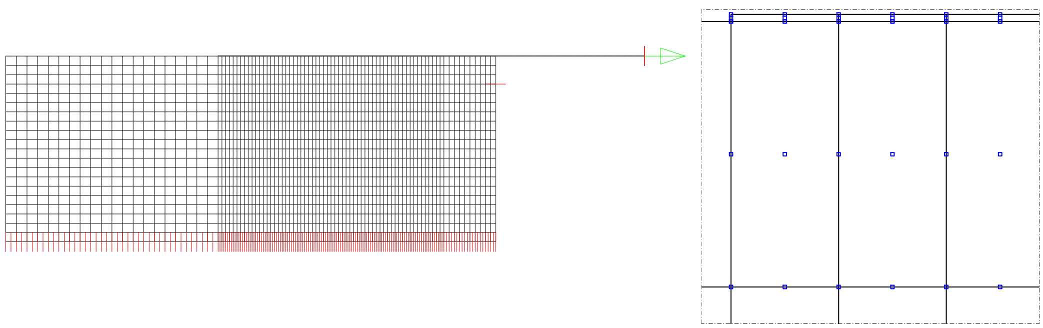

(a) (b)

Figure 20: (a) Two-dimensional finite element discretization of the FRP-concrete pull test. (b) Zoomed detail of the first FRP composite sheet elements.

the critical value of the Strain Energy Release Rate (SERR) for static delamination under pure mode I loading was evaluated as $G_{cr} = 0.26\,\mathrm{N\,mm^{-1}}$.

The fatigue tests were performed setting $R = P_{max}/P_{min} = 0.1$. The results of the fatigue tests were reported in Ref.[80] in terms of SERR that, according to the Bending beam loading and linear Fracture Mechanics Theory (BFMT), can be defined as function of the applied load P by the following relationship

$$G_I = \frac{12P^2a^2}{E_F b^2 h^3}. \tag{45}$$

In Ref.[80], the correction term proposed by Juntti *et al.* in Ref.[81] was added to the crack length.

The reference DCB test was computationally analysed employing a simplified two-dimensional finite element model where the composite was modelled by nine-node elements with orthotropic linear elastic material properties and the delamination surface was modelled by six-node interface elements associated with the proposed constitutive model. The interface constitutive parameters are collected in Table 2, where the fracture toughness G_I is related to the energy dissipated by damage only, as remarked in Section 3.1.1. The work of separation per unit surface under monotonic loading was computationally assessed testing an individual interface element and coincides with the critical SERR G_{cr}.

The results obtained for the monotonic quasi-static delamination simulation are reported in

Table 2: Interface properties for the FRP-concrete pull and DCB tests.

Property	Components	FRP-concrete	Carbon/epoxy
Interface properties			
Elastic-plastic limit strengths	t_n^{pl}, t_t^{pl}	8 MPa	10 MPa
Fracture toughness	G_{I}, G_{II}	$0.8\,\mathrm{N\,mm^{-1}}$	$0.24\,\mathrm{N\,mm^{-1}}$
Interface constitutive parameters			
Pure damage strengths	t_n^d, t_t^d	18.541 MPa	16.209 MPa
Pure damage critical displacement jumps	u_n^d, u_t^d	8.629×10^{-2} mm	2.961×10^{-2} mm
Endurance surface radii	r_n, r_t	0.6 MPa	1 MPa
Cohesive elastic stiffnesses	K_n, K_t	$226.172\,\mathrm{N\,mm^{-3}}$	$576.158\,\mathrm{N\,mm^{-3}}$
Cohesive hardening coefficients	C_n, C_t	$45.234\,\mathrm{N\,mm^{-3}}$	$288.079\,\mathrm{N\,mm^{-3}}$
Initial damage	ω_0	0.05	0.05
Damage-plasticity coupling parameter	a	0.25	0.035
Damage evolution parameter	m	6.5	3.5
Frictional coefficient	f	0	0

Fig.26 and compared with the BFMT analytical solution, exhibiting the well-known numerical instability issues in the descending delamination branch, see e.g. Ref. [25]. The critical delamination load for the monotonic numerical simulation was $P_{cr} = 49.74\,\mathrm{N}$.

The experimental fatigue analyses were performed for several values of the maximum applied load or, equivalently, for several values of the maximum SERR. The numerical simulations for the low-cycle fatigue analyses were performed only for three value of the maximum SERR, namely $G_1^{max} = 0.620\,G_{cr} = 0.1612\,\mathrm{N\,mm^{-1}}$, $G_2^{max} = 0.577\,G_{cr} = 0.15\,\mathrm{N\,mm^{-1}}$ and $G_3^{max} = 0.385\,G_{cr} = 0.10\,\mathrm{N\,mm^{-1}}$. The numerical simulations were performed with a cyclic load ranging from a maximum value P_{max} and a minimum value $P_{min} = 0.1\,P_{max}$. Due to the quadratic relationship between SERR and applied load P in Eq.45, the values of the maximum loads are $P_1 = \sqrt{0.62}\,P_{cr} \approx 40.79\,\mathrm{N}$, $P_2 = \sqrt{0.577}\,P_{cr} \approx 37.78\,\mathrm{N}$ and $P_3 = \sqrt{0.385}\,P_{cr} \approx 30.86\,\mathrm{N}$.

The load-displacement curves for the three numerical simulations are reported in Fig.26, where only the first loading cycles and the last ones before failure are represented, to facilitate the readability of the figure and avoid cramping it. The cyclic responses are compared with the monotonic response.

The crack initiation life, represented by the increasing length of the process zone, with the number of loading cycles for the three cyclic load cases is shown in Fig.27a. The evolution of the crack length with the number of loading cycles for the three cyclic load cases is shown in Fig.27b, where also the curve of the fatigue life is reported, highlighting a linear relation between load amplitude and number of cycles to failure, when the latter is reported in a logarithmic scale.

Eventually, the obtained numerical results are compared with the experimental outcomes in Fig.28, in terms of crack propagation rate *vs* SERR, where the latter has been evaluated as the average value during the first 5 mm crack propagation.

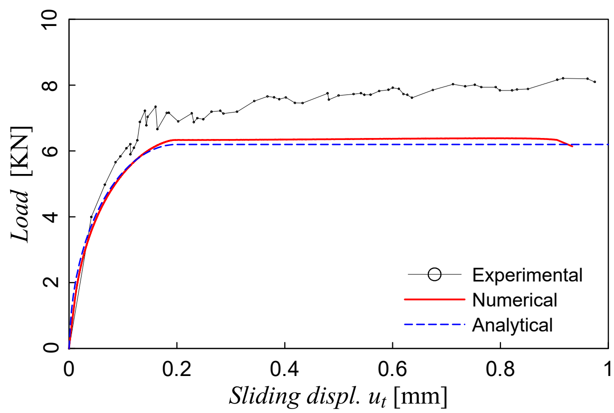

Figure 21: Numerical, analytical and experimental responses for the quasi-static monotonic FRP-concrete test in terms of applied load P *vs* sliding displacement u_t, performed under displacement control. The analytical solution is based on the theoretical formulation developed in Ref.[79].

4. Discussion and further developments

The performed computational tests have assessed the capabilities of the proposed formulation and confirmed its potential in the analysis of complex problems involving interfaces that may be the seat of initiation and evolution of irreversible damage, up to complete de-cohesion and failure.

Few observations about the proposed model are worthwhile. As discussed, for the analysis of low-cycle fatigue problems, the formulation suggests a coupling between the evolution of plasticity and damage. The coupling is introduced as a phenomenological mechanism linking the hysteretic accumulation of plasticity with the initiation and evolution of damage for traction states that do not overcome the pure damage activation threshold. However, the introduction of such phenomenological link requires the calibration of a certain number of parameters, see e.g. Table 2, which may not be readily available.

In the present work, the calibration has been performed according to the following procedure. The fracture energy and the interface traction strengths are inferred from experimental data, analogously to what is done in the literature with reference to pure-damage models. The pure damage strengths t_n^d, t_t^d and cohesive elastic stiffnesses K_n, K_t are defined as a function of both the fracture toughness $G_I = G_{II}$ and the interface strengths t_n^{pl}, t_t^{pl}, according to positions stated in Appendix A, for the intrinsic formulation, and by the approximate solutions given in Appendix B. The cohesive hardening coefficients C_n, C_t influence the *amplitude* of the hysteretic loading/un-loading cycles and the relevant energy dissipation; on the other hand, the hardening parameters, the damage-plasticity coupling parameter a and damage evolution parameter m govern the cyclic damage increments, the associated strength degradation, and the structural fatigue life. The calibration process of such parameters was performed in this work referring to available Wöhler S/N curves for the considered low-cycle fatigue tests. Once set, with reference to the calibration test, the selected materials properties were able to reproduce consistently also all the other performed tests, with different values of cyclic load amplitude. However, the formulation would benefit of explicit relationships between hysteretic plastic dissipation, cyclic damage increment and the number of loading cycles to failure; the exploration of such aspect is left to future investigations.

Another aspect that could be further developed is related to the assumption of identical mode I and II fracture toughnesses. Indeed, experimental evidence clearly shows higher values under shear tests, see e.g. Ref.[82]. A thermodynamically consistent formulation with independent fracture energies under the two loading conditions could be developed in a non-associative damage framework, with two independent damage variables, which would affect independently the normal and the tangential tractions, respectively. Examples of such an approach are proposed and discussed in Ref.[27], and could be extended to the formulation presented here, although the extension would be non-trivial and would require further assessment.

5. Conclusions

A novel thermodynamically consistent interface model for the analysis of low-cycle fatigue problems has been presented. The proposed interface relationships are developed starting from the definition of a suitable Helmholtz energy density function involving damage, plasticity, kinematical hardening and frictional variables. The central idea for capturing interface degradation under cyclic loading below the interface strength is to link the evolution of damage to some plastic hysteresis, so that also cycles with sub-critical amplitude may induce cyclic damage accumulation. The developed model has been computationally assessed with reference to an individual interface and two experimental low-cycle fatigue tests, involving composite joints in a pure mode II and a pure mode I case studies respectively. The obtained results show show that the model is able to produce physically consistent results and highlight the accuracy of the technique with respect to the experimental data. Further investigations could be focused on the calibration of the model and its extension to mixed-mode analyses with different fracture energies associated with mode I and II de-cohesion processes.

Acknowledgment

F.P. acknowledges the support of the Italian Ministry of Education, University and Research through the PRIN-2015 Project No. 2015LYYXA8, "*Multiscale mechanical models for the design and optimization of microstructured smart materials and metamaterials*".

I.B. acknowledges the support of the Italian Ministry of Education, University and Research through the project DEVISU, funded under the scheme PRIN-2107 – Grant 22017ZX9X4K_006.

Conflict of interest

The authors declare no potential conflict of interests.

Appendix A. Intrinsic implementation of the interface model

The extrinsic cohesive damage interface model described in Section 2.2 can be implemented in an intrinsic form, thus endowing the pristine interface with an initial elastic behaviour, by assuming a fictitious small value of damage $0 < \omega_0 \ll 1$. With the aim of preserving the assumed values of strength t_n^d and fracture energy, in this case the energy threshold should be re-defined as

$$Y_0 = \frac{K_n^{-1} {t_n^d}^2}{2\left(1-\omega_0\right)^2}, \tag{A.1}$$

while the critical opening and sliding displacement jumps would be $u_n^d = t_n^d/K_n/(1-\omega_0)$ and $u_t^d = t_t^d/K_t/(1-\omega_0)$, allowing to express the elastic stiffness parameters as functions of the fracture toughness and pure damage strengths as

$$K_n = \frac{{t_n^d}^2}{2G_{\mathrm{I}}(1-\omega_0)}, \qquad K_t = \frac{{t_t^d}^2}{2G_{\mathrm{II}}(1-\omega_0)}, \tag{A.2}$$

where $G_{\mathrm{I}} = G_{\mathrm{II}}$.

In the intrinsic formulation, the normal frictional stiffness can be assumed equal to the initial elastic stiffness ($K_n^f = K_n$), assuming the same tensile and compressive stiffness for the pristine interface. The frictional tangential stiffness may be assumed as $K_t^f \ll K_t$, so that the frictional behaviour can be neglected at the pristine condition.

Appendix B. Coupled plasticity-damage model response under monotonic loading

Under monotonic loading,the behaviour of the coupled plasticity-damage model approximates the response of pure damage cohesive models, due to the limited amount of plasticity, and associated damage, accumulated in monotonic processes.

The *interface strength* of the pristine interface under progressive monotonic loading cannot be analytically evaluated, due to the path dependency of the elastic-plastic response. However, since in monotonic loading the damage accumulated, due to plasticity-damage coupling, in the initial branch of the traction-opening curve is negligible, the interface strength can be estimated by enforcing the two activation conditions $\phi_d = 0$ and $\phi_p = 0$. Alternatively, the pure cohesive tensile strength t_n^d, which is a constitutive parameter in the pure damage model, can be defined as function of the normal and tangential elastic-plastic strengths

$$\begin{aligned} t_n^d &\approx \left[{t_n^{pl}}^2 + \frac{K_n}{C_n}\left(t_n^{pl} - r_n\sqrt{1-a}\right)^2 \right]^{\frac{1}{2}} (1-\omega_0) = \\ &= \left[\frac{K_n}{K_t}{t_t^{pl}}^2 + \frac{K_n}{C_t}\left(t_t^{pl} - r_t\sqrt{1-a}\right)^2 \right]^{\frac{1}{2}} (1-\omega_0), \end{aligned} \tag{B.1}$$

where the normal and tangential strengths, t_n^{pl} and t_t^{pl} respectively, are not independent of each other, being a unique fracture toughness value associated with both the opening and sliding failure modes.

Under the same assumption, i.e. by neglecting the damage increment induced by the plasticity-damage coupling in the initial elastic-plastic branch of the traction-opening curve, the pure mode I and mode II responses of the pristine interface can be estimated with acceptable approximation. For pure mode I monotonic loading, the initial behaviour is purely elastic with no hardening, $t_i^0 = 0$, and the plasticity-damage activation condition is reached when $t_n = t_3 \approx r_n$; in fact, for small values of traction, the energy release rate is $Y \ll Y_0$ and the last term in Eq.(23) can be neglected. Conversely, at the maximum strength, both yielding conditions are attained, $Y = Y^0$, and the actual radius of the endurance surface is $r_n\sqrt{1-a}$. Thus, the interface response is elastic-plastic up to the attainment of the damage activation condition and the maximum strength t_n^{pl} is reached with damage $\omega \approx \omega_0$. Eventually, the normal traction and the hardening parameter in the softening descending branch of the traction-displacement curve can be evaluated as function of damage, for $\omega \geq \omega_0$, by

$$t_n(\omega) \approx \left[\left(\frac{1-\omega}{1-\omega_0} \right)^2 \frac{C_n {t_n^d}^2}{K_n + C_n} - \frac{K_n C_n r_n^2}{(K_n + C_n)^2} (1-a) \right]^{\frac{1}{2}} + \frac{K_n r_n \sqrt{1-a}}{K_n + C_n}, \tag{B.2}$$

$$t_n^0(\omega) \approx \left[\left(\frac{1-\omega}{1-\omega_0} \right)^2 \frac{C_n {t_n^d}^2}{K_n + C_n} - \frac{K_n C_n r_n^2}{(K_n + C_n)^2} (1-a) \right]^{\frac{1}{2}} - \frac{C_n r_n \sqrt{1-a}}{K_n + C_n}, \tag{B.3}$$

while, employing Eqs.(8) and (13), the opening displacement and the plastic deformation can be expressed as

$$u_n(\omega) \approx \frac{\omega}{1-\omega} \left(t_n(\omega) \frac{K_n + C_n}{K_n C_n} - r_n \sqrt{1-a}/C_n \right), \tag{B.4}$$

$$u_n^p(\omega) \approx \frac{\omega}{1-\omega} t_n^0(\omega)/C_n. \tag{B.5}$$

The softening descending branch of the traction-separation curve under monotonic loading is initially associated with the coupled plasticity-damage behaviour whereas, for traction states approaching the endurance surface diameter, $2r_n\sqrt{1-a}$, the plastic evolution ceases and the residual behaviour is governed by pure damage evolution. The latter part of the curve before failure is approximately linear. The above considerations are numerically assessed in Section 3.1.1 and schematically summarised in Fig.6

The interface response under pure mode II monotonic loading can be also analysed by neglecting damage accumulation in the initial elastic-plastic branch and it exhibits a behaviour analogous to that described for mode I loading. The relevant static and kinematic components can be computed by considering the tangential components instead of the normal ones in Eqs.(B.2-B.5).

References

[1] J. Schijve, Fatigue of structures and materials in the 20th century and the state of the art, International Journal of Fatigue 25 (8) (2003) 679–702. doi:https://doi.org/10.1016/S0142-1123(03)00051-3.
URL https://www.sciencedirect.com/science/article/pii/S0142112303000513

[2] S. Bhaumik, M. Sujata, M. Venkataswamy, Fatigue failure of aircraft components, Engineering Failure Analysis 15 (6) (2008) 675–694. doi:https://doi.org/10.1016/j.engfailanal.2007.10.001.
URL https://www.sciencedirect.com/science/article/pii/S1350630707001409

[3] L. Kachanov, Introduction to continuum damage mechanics, Vol. 10, Springer Science & Business Media, 1986.

[4] D. Krajcinovic, J. Lemaitre, et al., Continuum damage mechanics: theory and applications, Springer, 1987.

[5] J. L. Chaboche, Continuum Damage Mechanics: Part I – General Concepts, Journal of Applied Mechanics 55 (1) (1988) 59–64. doi:10.1115/1.3173661.
URL https://doi.org/10.1115/1.3173661

[6] S. Murakami, Continuum damage mechanics: a continuum mechanics approach to the analysis of damage and fracture, Vol. 185, Springer Science & Business Media, 2012.

[7] T. L. Anderson, Fracture mechanics: fundamentals and applications, CRC press, 2017.

[8] R. H. Peerlings, R. de Borst, W. M. Brekelmans, J. de Vree, Gradient enhanced damage for quasi-brittle materials, International Journal for numerical methods in engineering 39 (19) (1996) 3391–3403.

[9] P. Paris, F. Erdogan, A critical analysis of crack propagation laws, J. bas. Engng. Trans. ASME, Ser. D 85 (1963) 528–533.

[10] M. Elices, G. Guinea, J. GÃşmez, J. Planas, The cohesive zone model: advantages, limitations and challenges, Engineering Fracture Mechanics 69 (2) (2002) 137–163. `doi:https://doi.org/10.1016/S0013-7944(01)00083-2`.
URL `https://www.sciencedirect.com/science/article/pii/S0013794401000832`

[11] B. Blackman, H. Hadavinia, A. J. Kinloch, J. Williams, The use of a cohesive zone model to study the fracture of fibre composites and adhesively-bonded joints, International Journal of fracture 119 (1) (2003) 25–46.

[12] J. Neumayer, H. Koerber, R. HinterhÃűlzl, An explicit cohesive element combining cohesive failure of the adhesive and delamination failure in composite bonded joints, Composite Structures 146 (2016) 75–83. `doi:https://doi.org/10.1016/j.compstruct.2016.03.009`.
URL `https://www.sciencedirect.com/science/article/pii/S0263822316301507`

[13] C. Sarrado, A. Turon, J. Costa, J. Renart, An experimental analysis of the fracture behavior of composite bonded joints in terms of cohesive laws, Composites Part A: Applied Science and Manufacturing 90 (2016) 234–242. `doi:https://doi.org/10.1016/j.compositesa.2016.07.004`.
URL `https://www.sciencedirect.com/science/article/pii/S1359835X16302238`

[14] V. P. Nguyen, M. Stroeven, L. J. Sluys, Multiscale continuous and discontinuous modeling of heterogeneous materials: a review on recent developments, Journal of Multiscale Modelling 03 (04) (2011) 229–270. `arXiv:https://doi.org/10.1142/S1756973711000509`, `doi:10.1142/S1756973711000509`.
URL `https://doi.org/10.1142/S1756973711000509`

[15] L. Bouhala, A. Makradi, S. Belouettar, H. Kiefer-Kamal, P. FrÃĺres, Modelling of failure in long fibres reinforced composites by x-fem and cohesive zone model, Composites Part B: Engineering 55 (2013) 352–361. `doi:https://doi.org/10.1016/j.compositesb.2012.12.013`.
URL `https://www.sciencedirect.com/science/article/pii/S1359836813003053`

[16] I. Benedetti, M. Aliabadi, Multiscale modeling of polycrystalline materials: A boundary element approach to material degradation and fracture, Computer Methods in Applied Mechanics and Engineering 289 (2015) 429–453. `doi:https://doi.org/10.1016/j.cma.2015.02.018`.
URL `https://www.sciencedirect.com/science/article/pii/S0045782515000675`

[17] V. Gulizzi, I. Benedetti, Micro-cracking of brittle polycrystalline materials with initial damage, European Journal of Computational Mechanics 25 (1-2) (2016) 38–53. `arXiv:https://doi.`

org/10.1080/17797179.2016.1181032, doi:10.1080/17797179.2016.1181032. URL https://doi.org/10.1080/17797179.2016.1181032

[18] V. Gulizzi, C. Rycroft, I. Benedetti, Modelling intergranular and transgranular micro-cracking in polycrystalline materials, Computer Methods in Applied Mechanics and Engineering 329 (2018) 168–194. doi:https://doi.org/10.1016/j.cma.2017.10.005. URL https://www.sciencedirect.com/science/article/pii/S0045782517306746

[19] J. McGarry, E. Ó Máirtín, G. Parry, G. Beltz, Potential-based and non-potential-based cohesive zone formulations under mixed-mode separation and over-closure. part I: Theoretical analysis, J. Mech. Physics Solids 63 (1) (2014) 336–362.

[20] D. Spring, O. Giraldo-Londoño, G. Paulino, A study on the thermodynamic consistency of the park paulino roesler (PPR) cohesive fracture model, Mechanics Research Communications 78 (2016) 100–109.

[21] K. Park, H. Choi, G. Paulino, Assessment of cohesive traction-separation relationships in abaqus: A comparative study, Mechanics Research Communications 78 (2016) 71–78.

[22] R. Dimitri, M. Trullo, G. Zavarise, L. De Lorenzis, A consistency assessment of coupled cohesive zone models for mixed-mode debonding problems, Frattura ed Integrita Strutturale 8 (29) (2014) 266–283.

[23] M. van den Bosch, P. Schreurs, M. Geers, An improved description of the exponential xu and needleman cohesive zone law for mixed-mode decohesion, Eng. Fract. Mech. 73 (9) (2006) 1220–1234.

[24] R. Serpieri, E. Sacco, G. Alfano, A thermodynamically consistent derivation of a frictional-damage cohesive-zone model with different mode I and mode II fracture energies, Eur. J. Mech., A/Solids 49 (2015) 13–25.

[25] G. Alfano, M. Crisfield, Finite element interface models for the delamination analysis of laminated composites: Mechanical and computational issues, Int. J. Num. Meth. Eng. 50 (7) (2001) 1701–1736.

[26] F. Parrinello, G. Marannano, G. Borino, A thermodynamically consistent cohesive-frictional interface model for mixed mode delamination, Engineering Fracture Mechanics 153 (2016) 61–79. doi:10.1016/j.engfracmech.2015.12.001.

[27] F. Parrinello, G. Borino, Non associative damage interface model for mixed mode delamination and frictional contact, European Journal of Mechanics / A Solids 76 (2019) 108–122.

[28] K. Park, G. Paulino, J. Roesler, A unified potential-based cohesive model of mixed-mode fracture, J. Mech. Physics Solids 57 (6) (2009) 891–908.

[29] F. Parrinello, G. Marannano, G. Borino, A. Pasta, Frictional effect in mode II delamination: Experimental test and numerical simulation, Eng. Fract. Mech. 110 (2013) 258–269.

[30] F. Parrinello, B. Failla, G. Borino, Cohesive-frictional interface constitutive model, Int. J. Solids Structures 46 (13) (2009) 2680–2692.

[31] F. Parrinello, G. Marannano, Cohesive delamination and frictional contact on joining surface via xfem, AIMS Materials Science 5 (1) (2018) 127–144. doi:10.3934/MATERSCI.2018.1.127.

[32] F. Parrinello, G. Borino, Integration of finite displacement interface element in reference and current configurations, Meccanica 53 (6) (2018) 1455–1468.

[33] G. Borino, F. Parrinello, A symmetric tangent stiffness approach to cohesive mechanical interfaces in large displacements, International Journal for Computational Methods in Engineering Science and Mechanics 0 (0) (2022) 1–16. doi:10.1080/15502287.2022.2032481.

[34] F. Parrinello, Analytical solution of the 4ENF test with interlaminar frictional effects and evaluation of mode II delamination toughness, Journal of Engineering Mechanics 144 (4). doi:10.1061/(ASCE)EM.1943-7889.0001433.

[35] G. Giambanco, E. La Malfa Ribolla, A. Spada, Meshless meso-modeling of masonry in the computational homogenization framework, Meccanica 53 (7) (2018) 1673–1697. doi:10.1007/s11012-017-0664-7.

[36] A. Spada, G. Giambanco, P. Rizzo, Damage and plasticity at the interfaces in composite materials and structures, Comp. Meth. Appl. Mech. Eng. 198 (49-52) (2009) 3884–3901.

[37] F. Parrinello, Hybrid equilibrium element with interelement interface for the analysis of delamination and crack propagation problems, International Journal for Numerical Methods in Engineeringdoi:10.1002/nme.6531.

[38] F. Parrinello, G. Borino, Hybrid equilibrium element with high-order stress fields for accurate elastic dynamic analysis, International Journal for Numerical Methods in Engineering 122 (21) (2021) 6308–6340. doi:https://doi.org/10.1002/nme.6793.

[39] I. Scheider, M. Pfuff, W. Dietzel, Simulation of hydrogen assisted stress corrosion cracking using the cohesive model, Engineering Fracture Mechanics 75 (15) (2008) 4283–4291. doi:https://doi.org/10.1016/j.engfracmech.2007.10.002.
URL https://www.sciencedirect.com/science/article/pii/S0013794407003724

[40] I. Benedetti, V. Gulizzi, A. Milazzo, Grain-boundary modelling of hydrogen assisted intergranular stress corrosion cracking, Mechanics of Materials 117 (2018) 137–151. doi:https://doi.org/10.1016/j.mechmat.2017.11.001.
URL https://www.sciencedirect.com/science/article/pii/S0167663617305276

[41] I. Benedetti, V. Gulizzi, A. Milazzo, A microstructural model for homogenisation and cracking of piezoelectric polycrystals, Computer Methods in Applied Mechanics and Engineering 357 (2019) 112595. doi:https://doi.org/10.1016/j.cma.2019.112595.
URL https://www.sciencedirect.com/science/article/pii/S0045782519304712

[42] O. Nguyen, E. Repetto, M. Ortiz, R. Radovitzky, A cohesive model of fatigue crack growth, International Journal of Fracture 110 (4) (2001) 351–369. doi:10.1023/A:1010839522926.

[43] K. Roe, T. Siegmund, An irreversible cohesive zone model for interface fatigue crack growth simulation, Engineering Fracture Mechanics 70 (2) (2003) 209–232. doi:10.1016/S0013-7944(02)00034-6.

[44] A. Needleman, An analysis of decohesion along an imperfect interface, International Journal of Fracture 42 (1) (1990) 21–40. doi:10.1007/BF00018611.

[45] Q. Yang, D. Shim, S. Spearing, A cohesive zone model for low cycle fatigue life prediction of solder joints, Microelectronic Engineering 75 (1) (2004) 85–95. doi:10.1016/j.mee.2003.11.009.

[46] S. Oller, O. Salomón, E. Oñate, A continuum mechanics model for mechanical fatigue analysis, Computational Materials Science 32 (2) (2005) 175–195. doi:10.1016/j.commatsci.2004.08.001.

[47] X. Martinez, S. Oller, L. Barbu, A. Barbat, A. de Jesus, Analysis of ultra low cycle fatigue problems with the barcelona plastic damage model and a new isotropic hardening law, International Journal of Fatigue 73 (2015) 132 – 142. doi:https://doi.org/10.1016/j.ijfatigue.2014.11.013.
URL http://www.sciencedirect.com/science/article/pii/S0142112314003016

[48] P. Carrara, L. D. Lorenzis, A coupled damage-plasticity model for the cyclic behavior of shear-loaded interfaces, Journal of the Mechanics and Physics of Solids 85 (2015) 33 – 53. doi:https://doi.org/10.1016/j.jmps.2015.09.002.

[49] P. Carrara, M. Ambati, R. Alessi, L. D. Lorenzis, A framework to model the fatigue behavior of brittle materials based on a variational phase-field approach, Computer Methods in Applied Mechanics and Engineering (2019) 112731doi:https://doi.org/10.1016/j.cma.2019.112731.

[50] M. Bocciarelli, A new cohesive law for the simulation of crack propagation under cyclic loading. application to steel- and concrete-frp bonded interface, Theoretical and Applied Fracture Mechanics 114 (2021) 102992. doi:https://doi.org/10.1016/j.tafmec.2021.102992.

[51] M. Costa, G. Viana, R. Créac'hcadec, L. da Silva, R. Campilho, A cohesive zone element for mode I modelling of adhesives degraded by humidity and fatigue, International Journal of Fatigue 112 (2018) 173–182. doi:https://doi.org/10.1016/j.ijfatigue.2018.03.014.

[52] J. Monteiro, A. Akhavan-Safar, R. Carbas, E. Marques, R. Goyal, M. El-zein, L. da Silva, Mode II modeling of adhesive materials degraded by fatigue loading using cohesive zone elements, Theoretical and Applied Fracture Mechanics 103 (2019) 102253. doi:https://doi.org/10.1016/j.tafmec.2019.102253.

[53] A. Rocha, A. Akhavan-Safar, R. Carbas, E. Marques, R. Goyal, M. El-zein, L. da Silva, Numerical analysis of mixed-mode fatigue crack growth of adhesive joints using CZM, Theoretical and Applied Fracture Mechanics 106 (2020) 102493. doi:https://doi.org/10.1016/j.tafmec.2020.102493.

[54] R. Dekker, F. van der Meer, J. Maljaars, L. Sluys, A cohesive XFEM model for simulating fatigue crack growth under mixed-mode loading and overloading, International Journal for Numerical Methods in Engineering 118 (10) (2019) 561–577. doi:https://doi.org/10.1002/nme.6026.

[55] R. H. J. Peerlings, W. A. M. Brekelmans, R. de Borst, M. G. D. Geers, Gradient-enhanced damage modelling of high-cycle fatigue, International Journal for Numerical Methods in Engineering 49 (12) (2000) 1547–1569. doi:https://doi.org/10.1002/1097-0207(20001230)49:12<1547::AID-NME16>3.0.CO;2-D.

[56] B. Coleman, W. Noll, The thermodynamics of elastic materials with heat conduction and viscosity, Arch. Rat. Mech. Analysis 13 (1963) 167–178.

[57] A. Risitano, G. Risitano, Cumulative damage evaluation of steel using infrared thermography, Theoretical and Applied Fracture Mechanics 54 (2) (2010) 82–90. doi:https://doi.org/10.1016/j.tafmec.2010.10.002.

[58] A. Risitano, G. Risitano, Cumulative damage evaluation in multiple cycle fatigue tests taking into account energy parameters, International Journal of Fatigue 48 (2013) 214–222. doi:https://doi.org/10.1016/j.ijfatigue.2012.10.020.

[59] Q. Guo, F. Zaïri, X. Guo, An intrinsic dissipation model for high-cycle fatigue life prediction, International Journal of Mechanical Sciences 140 (2018) 163–171. doi:https://doi.org/10.1016/j.ijmecsci.2018.02.047.

[60] S. Zhang, Y. Xu, H. Fu, Y. Wen, Y. Wang, X. Liu, Low-cycle fatigue crack initiation simulation and life prediction of powder superalloy considering inclusion-matrix interface debonding, Materials 14 (14) (2021) 4018.

[61] M. J. Mahtabi, N. Shamsaei, A modified energy-based approach for fatigue life prediction of superelastic NiTi in presence of tensile mean strain and stress, International Journal of Mechanical Sciences 117 (2016) 321–333. doi:https://doi.org/10.1016/j.ijmecsci.2016.08.012.

[62] A. Corigliano, Formulation, identification and use of interface models in the numerical analysis of composite delamination, Int. J. Solids Structures 30 (20) (1993) 2779–2811.

[63] L. Daudeville, O. Allix, P. Ladevéze, Delamination analysis by damage mechanics: Some applications, Comp. Engng 5 (1) (1995) 17–24.

[64] O. Allix, P. LadevÃĺze, A. Corigliano, Damage analysis of interlaminar fracture specimens, Comp. Struct. 31 (1) (1995) 61–74.

[65] A. Corigliano, O. Allix, Some aspects of interlaminar degradation in composites, Comp. Meth. Appl. Mech. Eng. 185 (2-4) (2000) 203–224.

[66] J. Mosler, I. Scheider, A thermodynamically and variationally consistent class of damage-type cohesive models, J. Mech. Physics Solids 59 (8) (2011) 1647–1668.

[67] G. Alfano, E. Sacco, Combining interface damage and friction in a cohesive-zone model, Int. J. Num. Meth. Eng. 68 (5) (2006) 542–582.

[68] R. Serpieri, G. Alfano, Bond-slip analysis via a thermodynamically consistent interface model combining interlocking, damage and friction, Int. J. Num. Meth. Engng. 85 (2) (2011) 164–186.

[69] I. Guiamatsia, G. Nguyen, A thermodynamics-based cohesive model for interface debonding and friction, Int. J. Solids Structures 51 (3-4) (2014) 647–659.

[70] I. Benedetti, M. Aliabadi, A three-dimensional cohesive-frictional grain-boundary micromechanical model for intergranular degradation and failure in polycrystalline materials, Computer Methods in Applied Mechanics and Engineering 265 (2013) 36–62. doi:https://doi.org/10.1016/j.cma.2013.05.023.
URL https://www.sciencedirect.com/science/article/pii/S0045782513001503

[71] M. E. Gurtin, E. Fried, L. Anand, The Mechanics and Thermodynamics of Continua, Cambridge University Press, 2010. doi:10.1017/CBO9780511762956.

[72] I. Benedetti, V. Gulizzi, A grain-scale model for high-cycle fatigue degradation in polycrystalline materials, International Journal of Fatigue 116 (2018) 90 – 105. doi:https://doi.org/10.1016/j.ijfatigue.2018.06.010.
URL http://www.sciencedirect.com/science/article/pii/S0142112318302287

[73] Y.-C. Xiao, S. Li, Z. Gao, A continuum damage mechanics model for high cycle fatigue, International Journal of Fatigue 20 (7) (1998) 503 – 508. doi:https://doi.org/10.1016/S0142-1123(98)00005-X.
URL http://www.sciencedirect.com/science/article/pii/S014211239800005X

[74] B. Hajshirmohammadi, M. Khonsari, An approach for fatigue life prediction based on external heating, International Journal of Mechanical Sciences 204 (2021) 106510. doi:https://doi.org/10.1016/j.ijmecsci.2021.106510.

[75] O. Zienkiewicz, Taylor, The Finite Element Method. 5th Edition, Butterworth-Heinemann Press, 2000.

[76] C. Carloni, K. V. Subramaniam, M. Savoia, C. Mazzotti, Experimental determination of frpâĂŞconcrete cohesive interface properties under fatigue loading, Composite Structures 94 (4) (2012) 1288–1296. doi:https://doi.org/10.1016/j.compstruct.2011.10.026.
URL https://www.sciencedirect.com/science/article/pii/S0263822311004065

[77] E. Martinelli, A. Caggiano, Low-cycle fatigue of FRP strips glued to a quasi-brittle material, Materials 14 (24). doi:10.3390/ma14247753.
URL https://www.mdpi.com/1996-1944/14/24/7753

[78] A. Caggiano, E. Martinelli, C. Faella, A fully-analytical approach for modelling the response of FRP plates bonded to a brittle substrate, International Journal of Solids and Structures 49 (17) (2012) 2291–2300. doi:https://doi.org/10.1016/j.ijsolstr.2012.04.029.

[79] L. E. Asp, A. Sjögren, E. S. Greenhalgh, Delamination growth and thresholds in a carbon/epoxy composite under fatigue loading, Journal of Composites Technology & Research 23 (2) (2001) 55–68. doi:DOI:10.1520/CTR10914J.

[80] M. Juntti, L. E. Asp, R. Olsson, Assessment of evaluation methods for the mixed-mode bending test, Journal of Composites Technology & Research 21 (1) (1999) 37–48. doi:DOI:10.1520/CTR10611J.

[81] M. L. Benzeggagh, M. Kenane, Measurement of mixed-mode delamination fracture toughness of unidirectional glass/epoxy composites with mixed-mode bending apparatus, Compos. Sci. Technol. 56 (1996) 439–449.

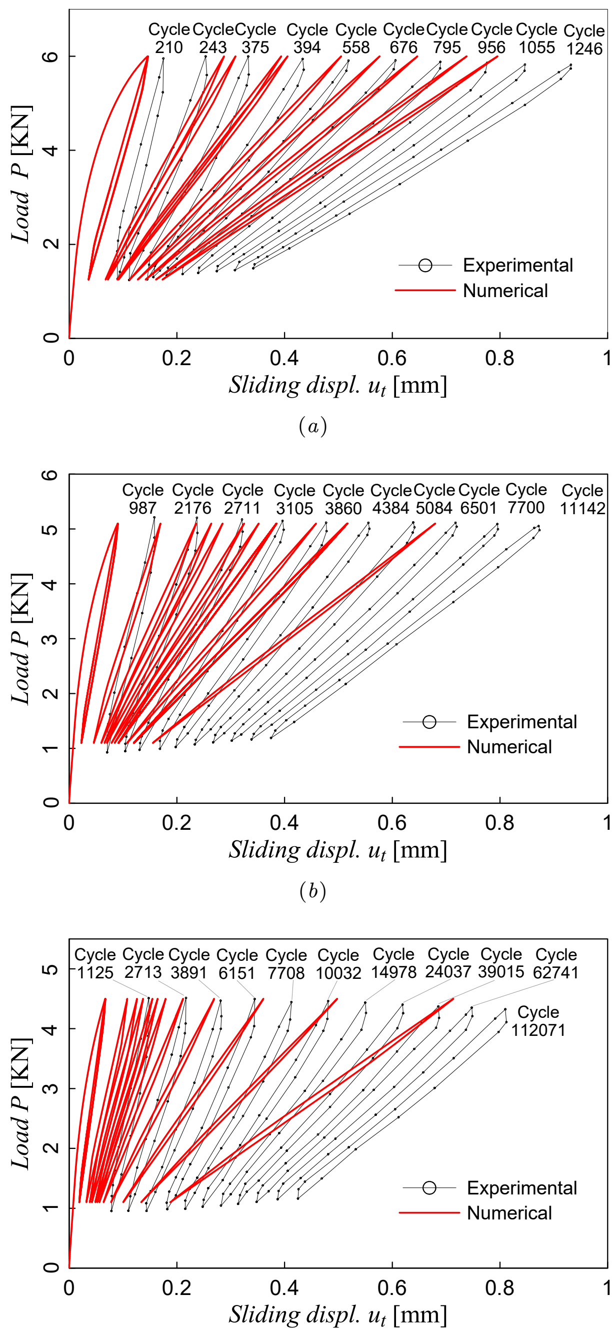

Figure 22: Numerical and experimental [77] responses for: (a) the first cyclic test DS-F1; (b) the second cyclic test DS-F2; (c) the third cyclic test DS-F3; in terms of applied load P *vs* sliding displacement u_t, performed under load control. The responses are plotted for some significant loading cycles.

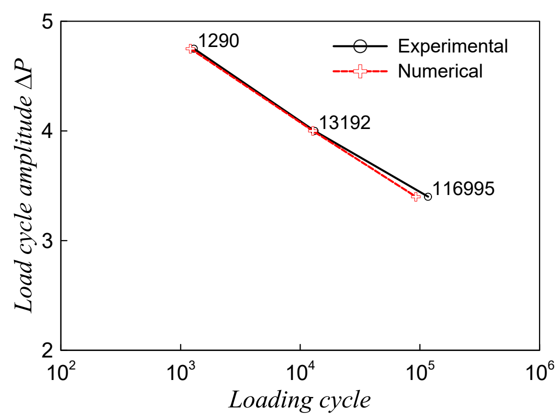

Figure 23: Fatigue life in terms of load cycle amplitude ΔP *vs* number of cycle to failure, in logarithmic scale. The computationally estimated fatigue life is compared with the experimental data given in Ref.[77].

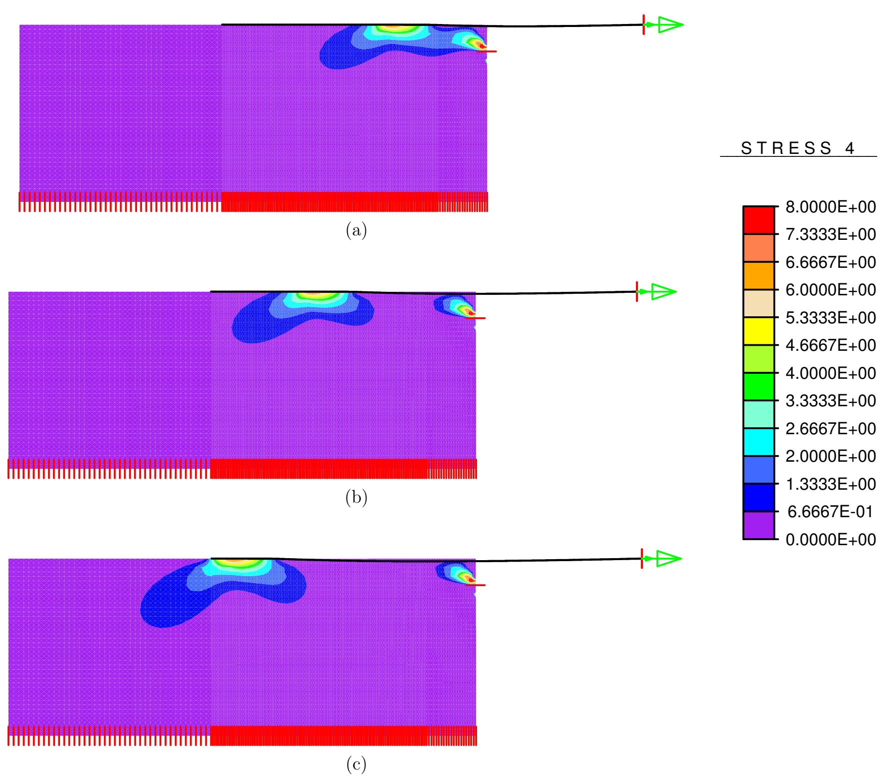

Figure 24: Tangential stress maps for the pull cyclic test, at the peak of the load cycles: (a) 75; (b) 575; (c) 1175.

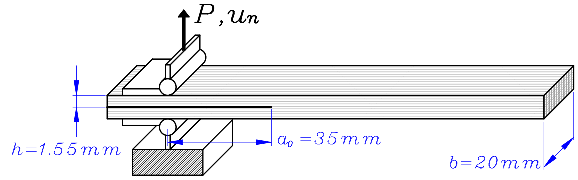

Figure 25: Set-up and dimensions of the end notched carbon/epoxy composite specimen in a classic Double Cantilever Beam (DCB) test..

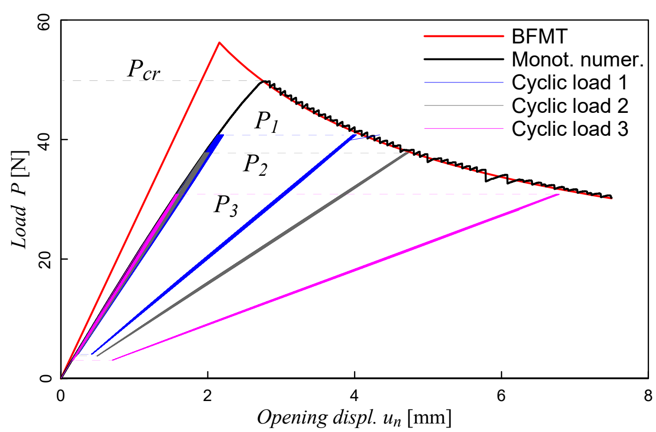

Figure 26: Load-displacement curves of the carbon-epoxy DCB test, for the monotonic quasi-static analysis and for the three performed cyclic-load tests. The monotonic response is compared to the analytical solution developed under the hypothesis of linear elastic Beam theory and elastic Fracture Mechanics Theory (BFMT). The responses of the three cyclic tests are plotted only for the first loading cycles and for the last cycles before failure.

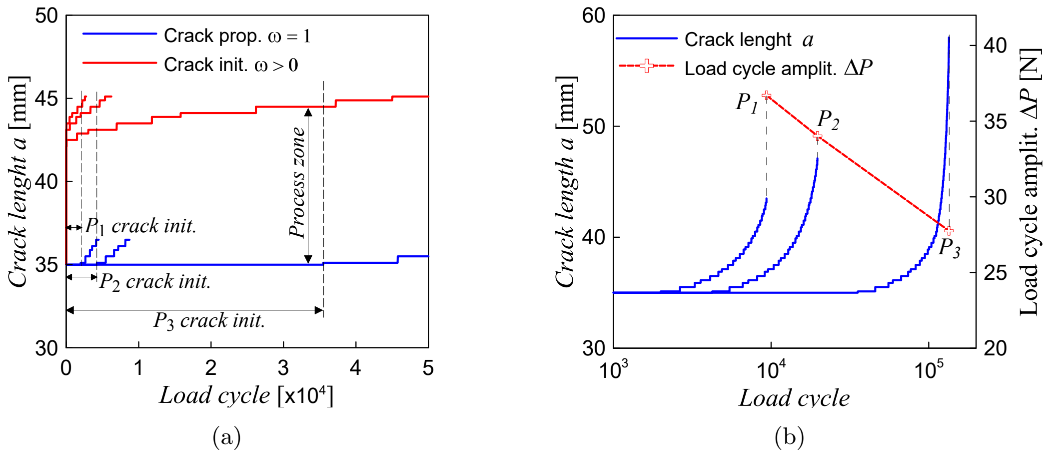

Figure 27: (a) The crack initiation life under the three cyclic load cases is represented by the *process zone* ($0 < \omega < 1$) which enlarges up to the full damage condition is achieved and the crack starts to propagate. (b) Crack propagation during the three low-cycle fatigue tests and fatigue life *vs* load cycle amplitude.

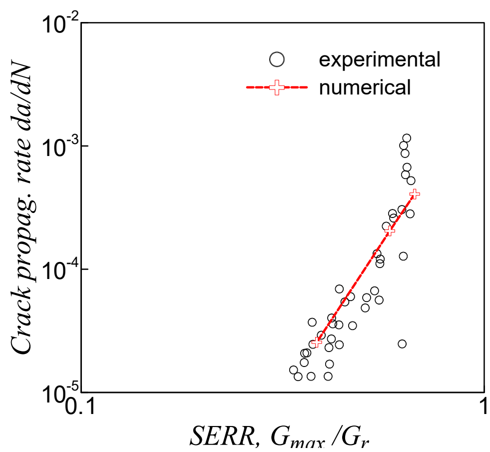

Figure 28: Crack propagation rate *vs* relative SERR G_{max}/G_{cr} at the maximum applied load during the cyclic load, compared with the experimental results reported in Ref. [80] The crack propagation rate is evaluated as average value of the rate in the first 5mm of crack propagation.